Water Resources Research

RESEARCH ARTICLE
10.1029/2022WR032829

Using Noncontact Measurement of Water Surface Dynamics to Estimate River Discharge

G. Dolcetti[1,2], B. Hortobágyi[3], M. Perks[3], S. J. Tait[1], and N. Dervilis[4]

[1]Department of Civil and Structural Engineering, The University of Sheffield, Sheffield, UK, [2]Now at Department of Civil, Environmental and Mechanical Engineering, University of Trento, Trento, Italy, [3]School of Geography, Politics and Sociology, Newcastle University, Newcastle, UK, [4]Department of Mechanical Engineering, The University of Sheffield, Sheffield, UK

Key Points:

- Water surface fluctuations of a river surface react systematically to changes in the flow depth and velocity
- Depth, velocity, and discharge are estimated remotely by fitting theoretical relations to the spectra of images of the water surface
- The uncertainty of the estimates is governed by the size of river surface covered by the images, limiting the achievable spatial resolution

Correspondence to:
S. J. Tait,
s.tait@sheffield.ac.uk

Citation:
Dolcetti, G., Hortobágyi, B., Perks, M., Tait, S. J., & Dervilis, N. (2022). Using noncontact measurement of water surface dynamics to estimate river discharge. *Water Resources Research*, *58*, e2022WR032829. https://doi.org/10.1029/2022WR032829

Received 19 MAY 2022
Accepted 7 SEP 2022

Abstract Estimating river discharge requires simultaneous measurement of velocity and flow depth. While surface velocities are relatively easy to measure using noncontact techniques, depth measurement usually requires physically intrusive instrumentation. This limits our capability to remotely monitor discharge in natural rivers subject to bed level variations. This work tests the potential to estimate the surface velocity, the water depth, the depth average velocity, and then discharge of a river using only a sequence of images of the dynamic water surface. The method is based on a comparison between the spatiotemporal Fourier spectra of the pixel intensities of these images and the theoretical dispersion relations of turbulence-generated surface fluctuations and gravity-capillary waves. The method is validated through the analysis of water surface videos obtained with fixed cameras from two river sections equipped with conventional discharge gauging. The applicability of the approach is demonstrated and the measurement uncertainties are quantified. The method is affected by two main sources of uncertainty: one derives from the estimation of the velocity index and the other from the obtainable resolution of the Fourier analysis. This resolution strongly controls the observation of depth and/or velocity variations in space and in time. The technique has advantages over current approaches: it has clear physical foundations; the equipment is low cost and is highly mobile; it does not need artificial tracers or physical equipment to measure depth; and it can directly provide estimates of the key flow parameters just from time series of images of the water surface.

Plain Language Summary Continuous river flow discharge measurement is of great importance for managing natural water resources and flood risks. Current remote measurements that can be performed without immersing sensors only determine the velocity of the very upper surface layer of the river. River water surfaces have distinct patterns of waves. This work demonstrates that by remotely observing the dynamics of water surface waves using a low-cost video camera and using wave theory, it is possible to estimate the surface water velocity, water depth, depth-average velocity, and therefore the flow rate.

1. Introduction

Noncontact measurement techniques are increasingly used to monitor rivers, especially in flood events, when traditional flow gauging techniques are difficult to apply (e.g., Le Coz et al., 2010; Perks et al., 2016). Existing noncontact techniques have been used almost exclusively for measuring the surface flow velocity pattern, using radar or ultrasound scattering from the water surface (e.g., Dolcetti et al., 2017; Plant et al., 2005; Welber et al., 2016), or tracking floating tracer particles or surface ripples with cameras (e.g., Fujita & Tsubaki, 2002; Muste et al., 2005; Perks et al., 2016; Tauro et al., 2017). Measuring river discharge using only noncontact instrumentation is challenging, mainly because of the difficulty in estimating the water depth. Relative variations of the typical water level can be quantified based on images of the intersection of the water-air interface with the river banks (e.g., D. S. Young et al., 2015; Eltner et al., 2018). However, the estimation of the water depth requires determination of the bed level, which could change significantly, especially during and after flood events (Johnson & Cowen, 2016).

Direct measurements of the bathymetry based on ground penetrating radar (Spicer et al., 1997) or terrestrial laser scanners (Smith et al., 2012) can measure complex channel shapes, but they are expensive and energy demanding and so are difficult to deploy (Detert et al., 2017). Techniques based on water color or photogrammetry are limited to shallow, clear water (Woodget et al., 2015). Techniques to estimate the discharge based solely on the surface

velocity distributions have been proposed, for example, by Bradley et al. (2002), Gharahjeh and Aydin (2016), Yang et al. (2019). However, these methods require a site-specific calibration based on a previous survey of the measurement site in similar conditions (i.e., without significant changes of the bed level). A method described by Moramarco et al. (2019) estimates the bathymetry (and the discharge) by fitting the measured surface velocity profile with a model based on entropy theory. Johnson and Cowen (2016) and Jin and Liao (2019) proposed to exploit an empirical correlation between the water depth and the statistics of turbulence at the water surface. Turbulence measurements in the field using Large Scale Particle Image Velocimetry (LSPIV) require a high density of tracers, and velocity measurement can be uncertain in the presence of water waves (e.g., Dolcetti et al., 2020; Tauro et al., 2014). The method presented here is complementary to the empirical approaches of Johnson and Cowen (2016) and Jin and Liao (2019), it is theoretically grounded and is specifically developed to take account of the presence of dynamic water surface waves.

In the ocean, the propagation velocity of wind-generated surface gravity waves is known to change with depth and with currents. Therefore, the current velocity (I. R. Young et al., 1985; Senet et al., 2001), the vertical profile of velocity (Campana et al., 2016; Lund et al., 2015; Stewart & Joy, 1974), and the water depth (Bell, 1999; Dugan et al., 2001) are all quantities that can be estimated indirectly based on spatiotemporal measurements of the ocean surface dynamics which can be obtained by radar, cameras, or even satellite images (Salameh et al., 2019). In turbulent open channel flows, various laboratory studies (Dolcetti et al., 2016; Savelsberg & Van De Water, 2009) have highlighted the presence of water surface gravity and gravity-capillary waves, with a velocity of propagation that can be predicted by analytical models (Dolcetti & García Nava, 2019b; Dolcetti et al., 2016). This knowledge allows for use of approaches derived originally for ocean waves (e.g., Serafino et al., 2009) to wave types that form at the surface of shallow river flows.

The approach followed here is based on fitting of the three-dimensional (2D-spatial and 1D-temporal) spatiotemporal spectrum of the local water surface slope to an analytical wave model. Streβer et al. (2017) were the first to use a similar approach in rivers, but their application was limited to the estimation of the surface velocity. Here, mean surface velocity and water depth are determined simultaneously from noncontact measurements of the water surface motion. Based on the velocity-area method (e.g., Welber et al., 2016), an estimate of the discharge can be obtained, Q, as

$$Q = \sum_{j}^{N} \alpha_j U_j d_j w_j, \tag{1}$$

where U_j is the time-averaged surface velocity, d_j is the water depth, α_j is the velocity index (the ratio between the depth-averaged flow velocity and the surface velocity), and the index j denotes that each quantity is measured at the jth location along a transect, over a sub-section of width w_j, where $W = \sum_j^N w_j$ is the river width, and N is the number of sub-sections. In practice, the spatial resolution of the proposed analysis method allowed only one estimate per river cross-section, therefore the flow rate had to be estimated based on the equation below

$$Q = \alpha U_0 d W, \tag{2}$$

where α, U_0, and d represent the average velocity-index, surface velocity, and water depth, for an area with width comparable to W.

The validity of the approach was tested using several videos recorded at two sites for which measurements of the depth and discharge were obtained using fixed conventional gauging installations. The river sections selected for this study were heavily modified, relatively steep, with coarse gravel beds, and trapezoidal channel sections. These conditions are considered to provide a reasonable environment for the method validation, since they yield visible water surface deformations and relatively simple velocity distributions while being at "field scale" in terms of Reynolds and Froude numbers.

This work is structured as follows: Section 2 summarizes the equations that describe the dynamics of water surfaces in an idealized channel; Section 3 describes how a Fourier analysis of image sequences of the river surface can measure surface dynamics, and how to infer flow properties using the equations introduced in Section 2; Section 4 examines measurement uncertainty; Section 5 describes the measurement sites, and presents some example water surface Fourier spectra; Section 6 presents a comparison of the quantities of the flow estimated with the proposed approach and measured with traditional gauging equipment; Section 7 discusses the

accuracy and scalability of this approach; Section 8 summarizes the conclusion; Appendix A provides some additional details about the fitting algorithm used for this work; and Appendix B reports the full equations that describe the sensitivity of the dispersion relation of gravity-capillary waves from variations of the surface velocity and water depth.

2. Water Surface Dynamics in Rivers

2.1. Types of Water Surface Deformations

Free surface deformations in rivers can be caused by a variety of phenomena, such as turbulence, shear instabilities, and wind (Brocchini & Peregrine, 2001; Muraro et al., 2021). They are usually divided into two categories, based on their appearance and dynamics: deformations forced locally by the action of turbulent structures within the flow, and freely propagating gravity-capillary (GC) waves (Brocchini & Peregrine, 2001; Teixeira & Belcher, 2006). Turbulence-forced deformations can have the form of local 2D (scars) or 1D (vortex dimples) surface indentations above vortex filaments (e.g., Sarpkaya, 1996), or they can appear as patches of divergent surface flow with a smoother surface but with well-defined, rough margins, often populated with short capillary ripples (Longuet-Higgins, 1996). The occurrence of these patches has been linked to strong surface-renewal eddies in highly turbulent flows (often called boils, e.g., Nezu and Nakagawa, 1993). Known causes of GC waves, on the other hand, include wind, rain drops, or emerging obstacles and vegetation that produce characteristic oblique "wake-like" patterns. GC waves can also be created by turbulence-forced deformations, or they can grow due to a resonance with turbulence pressure fluctuations in a sheared flow (Teixeira & Belcher, 2006). GC waves that appear to be fixed in space and in time (called stationary or standing waves) are known to form at near critical Froude numbers over rough beds (Chanson, 2000), and they were also found to dominate free-surface spatial and temporal scales at relatively low Froude numbers $\mathsf{F} \sim 0.2$ (Dolcetti et al., 2016). These waves can exchange energy with the turbulent flow to promote the growth of other, nonstationary, GC waves, and the resulting patterns seem to represent the main type of surface deformation for a wide range of subcritical Froude numbers (Dolcetti & García Nava, 2019b; Muraro et al., 2021).

2.2. Dispersion Relations

GC waves are distinguished from turbulence-generated surface deformations (i.e., boils, scars, etc.) because they appear periodic at least in one spatial dimension. However, groups of waves with different wavelengths and directions can combine and form rather complex patterns. A quantitative separation of the two types of surface deformations is based on a Fourier analysis of the surface-elevation data in space and in time (e.g., Dolcetti et al., 2016; Savelsberg & Van De Water, 2009), which decomposes the data in a series of plane waves, each with a radian frequency $\omega = 2\pi f$, where f is the frequency in Hz, and with a wavenumber vector $\mathbf{k}$, where $k = |\mathbf{k}| = 2\pi/\lambda$, λ is the wavelength, and $\mathbf{k}$ is orthogonal to the wave crest. The ratio between the frequency and wavenumber, $c = \omega/k$ is the speed of propagation (phase speed) of a wave, and the relation $\omega = \Omega(\mathbf{k})$ is called the dispersion relation.

A Fourier analysis can be applied to any type of surface deformations, including turbulence-generated ones. If the mean speed of the flow is faster than the speed at which the patterns deform, the temporal fluctuations of the surface elevation at a fixed point is due primarily to advection and the wavenumber-frequency relation can be approximated by (Dolcetti et al., 2016)

$$\omega \approx \Omega_A(\mathbf{k}, \mathbf{U}_0) = \mathbf{k} \cdot \mathbf{U}_0. \tag{3}$$

Ω_A represents the advection of the surface patterns at a constant velocity. In this case, the surface deformations are believed to travel at the same speed as the turbulent structures that cause them, which is close to the average speed of the flow near the surface, U_0.

GC waves, on the other hand, propagate relative to the mean flow, and their speed changes with the wavelength. The dispersion relation for GC waves in still water with depth d is (e.g., Lamb, 1945, p. 459)

$$\omega = \Omega_i(k, d) = k\sqrt{gd\frac{(1+\mathsf{B})}{\mathsf{B}}\frac{\tanh(kd)}{kd}}, \tag{4}$$

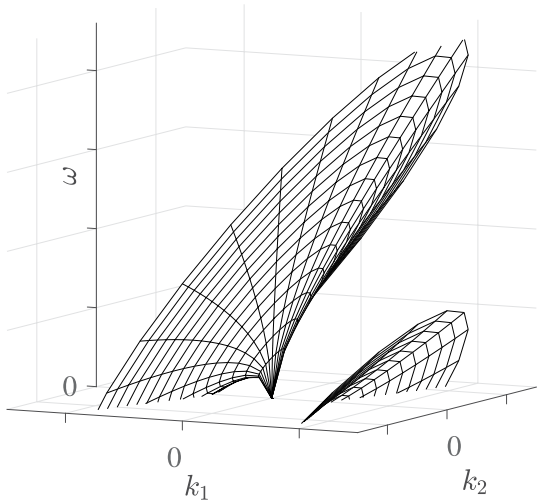

Figure 1. 3D Dispersion relation of gravity-capillary waves, Equation 6. Here, k_1 is in the direction of the flow.

where $\mathsf{B} = \rho g / \left(k^2 \gamma\right)$ is the Bond number, which indicates the ratio of gravity and surface tension effects, g is the acceleration due to gravity, γ is the surface tension coefficient, and ρ is the water density.

$\Omega_i(k, d)$ is often called the intrinsic wave frequency, since it does not include the effects of the mean flow, and it does not depend on the direction of propagation. When the speed of the flow beneath the waves varies along the vertical co-ordinate, $U = U(z)$, the dispersion relation varies nontrivially. Specific formulations have been derived for power-function velocity profiles (Fenton, 1973), or for profiles with arbitrary shape (e.g., Ellingsen & Li, 2017), but they all require the numerical solution of an implicit equation. Apparently the only way to make the problem explicit and practicable for solution is to approximate the vertical profile of the streamwise velocity with a linear profile,

$$U(z) = \left(m\frac{z}{d} + q\right) U_0, \tag{5}$$

where m is the vertical gradient of streamwise velocity and $q = 1 - m$, so that $U_0 = U(d)$ is the speed at the surface. For the velocity profile of Equation 5, the dispersion relation can be calculated explicitly as (e.g., Biésel, 1950; Teixeira & Belcher, 2006)

$$\omega = \Omega_{\mathrm{GW}}\left(\mathbf{k}, \mathbf{U}_0, d\right) = \left[1 - \beta(k, d)\right] \Omega_{\mathrm{A}}\left(\mathbf{k}, \mathbf{U}_0\right) \pm \sqrt{\left[\beta(k, d)\Omega_{\mathrm{A}}\left(\mathbf{k}, \mathbf{U}_0\right)\right]^2 + \Omega_{\mathrm{i}}^2(k, d)}, \tag{6}$$

where

$$\beta(k, d) = \frac{m}{2}\frac{\tanh(kd)}{kd}. \tag{7}$$

The $\pm$ sign in Equation 6 indicates the two waves with opposite direction of propagation.

Equation 6 is plotted in Figure 1 as a function of the two components of the wavenumber vector k_1 and k_2 aligned with the horizontal coordinates x_1 and x_2, respectively, for a case where x_1 is in the direction of the flow, that is, $\mathbf{U}_0 = (U_0, 0) = U_0\mathbf{e}_1$. The two solutions with opposite signs correspond to two surfaces that can intersect the $\omega = 0$ plane for certain combinations of k_1 and k_2.

All waves with $\omega = 0$ are stationary waves. Among these, the stationary waves with the crest perpendicular to the flow ($k_2 = 0$) are of importance because they define the representative scale of water surface deformations for turbulent flows over rough beds in the laboratory and in the field (Dolcetti & García Nava, 2019b; Dolcetti et al., 2016; Muraro et al., 2021). The wavenumber of these stationary waves, k_0, is found from the solution of $\Omega_{\mathrm{GW}}(\mathbf{k}, \mathbf{U}_0, d) = 0$ for a case with $\mathbf{k}_0 \cdot \mathbf{U}_\mathbf{0} = -k_0 U_0$, which results in

$$k_0 d = \left[m + \frac{1}{\mathsf{F}^2}\frac{(1 + \mathsf{B})}{\mathsf{B}}\right] \tanh(k_0 d), \quad \rightarrow \quad \frac{\lambda_0}{d} = \frac{2\pi\mathsf{F}^2}{\left[(1 + \mathsf{B})/\mathsf{B} + m\mathsf{F}^2\right] \tanh(2\pi d/\lambda_0)}, \tag{8}$$

where $\lambda_0 = 2\pi/k_0$ is a characteristic wavelength. Equation 8 will be used for estimating the horizontal scale of water waves while quantifying the measurement uncertainties in Section 4. In the deep-water gravity wave limit ($k_0 d \gg 1, \mathsf{B} \gg 1$) it is simplified as (Teixeira, 2019)

$$k_0 d = m + \frac{1}{\mathsf{F}^2} \quad \rightarrow \quad \frac{\lambda_0}{d} = \frac{2\pi\mathsf{F}^2}{1 + m\mathsf{F}^2}. \tag{9}$$

The dispersion relationships of turbulence-generated water surface fluctuations and of GC waves depend on the flow parameters, namely the flow surface speed U_0, and the depth d. This dependence is exemplified in Figures 2a and 2b, and in Figures 2c and 2d, respectively. The results in Figures 2a and 2c are for waves that propagate parallel to the flow ($k = k_1, k_2 = 0$), while those in Figures 2b and 2d are for orthogonal direction of propagation ($k = k_2, k_1 = 0$). $\Omega_{\mathrm{A}}(k_1)$ increases linearly with U_0, and is independent of d. As U_0 increases, $\Omega_{\mathrm{GW}}(k_1)$ increases for

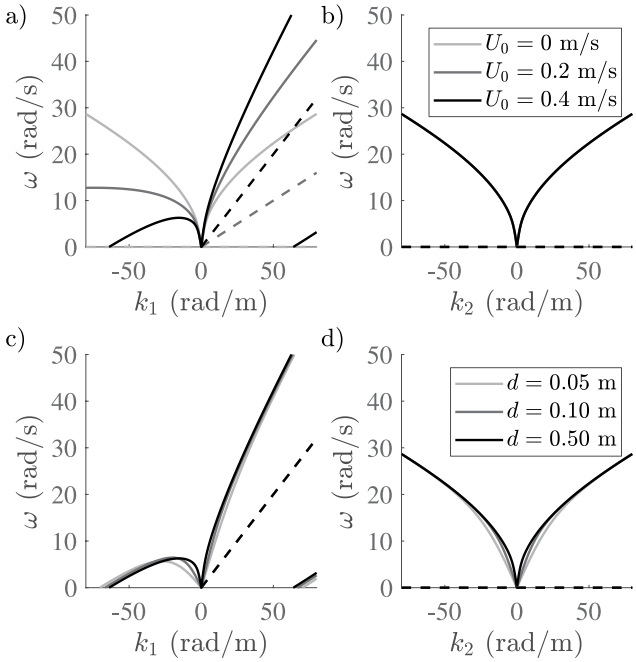

Figure 2. Effect of (a and b) flow velocity and (c and d) depth on the frequency of (solid lines) gravity-capillary waves and (dashed lines) turbulence-generated surface deformations. (a and c) Waves are parallel to the flow direction, $k = k_1$, $k_2 = 0$. (b and d) Waves are perpendicular to the flow direction, $k = k_2$, $k_1 = 0$. Example calculated for $m = 0.34$. (a and b) $d = 0.5$ m. (c and d), $U_0 = 0.4$ m/s.

the waves that propagate downstream ($k_1 > 0$), and decreases for the waves that propagate upstream ($k_1 < 0$) (see Figure 2a). Since Ω_{GW} depends on the inner product $\mathbf{k} \cdot \mathbf{U}_0$, the waves that propagate orthogonally with respect to the flow are not affected by the flow velocity, therefore $\Omega_{GW}(k_2)$ is independent of U_0 (see Figure 2b). Depth variations have a smaller effect, but they affect the frequency of all GC waves, including those that propagate perpendicularly to the flow. For these waves, $\Omega_{GW}(k_2)$ increases with the depth. This is more evident at low wavenumbers (long waves), as shown in Figure 2d. The effect on the waves that propagate parallel to the flow, shown in Figure 2c is more difficult to generalize because of the nontrivial dependence of β and Ω_i on d.

3. Remote Estimation of Flow Parameters

3.1. Measurement of Water Surface Deformations From Video Images

The analysis described below can be applied to water surface elevation measurements obtained with different sensing technologies, for example, with radar (Shen et al., 2015), with ultrasound (Krynkin et al., 2016), or optically (Benetazzo et al., 2018). In practice, direct measurements of the water surface shape over an area comparable to the river width, with high spatial and temporal resolution, are difficult to obtain. Variations of the spatial gradient of the water surface (surface slope) in time can be observed using low cost cameras. The technique has been used in oceanography for a long time (Williams, 1947). Two phenomena contribute mostly to the intensity of light that reaches the camera from a certain region in space after having been reflected from a water surface: the dependence of the brightness of the sky from the azimuth angle and the variation of light reflectivity at the water surface. The color of a clear or uniformly cast sky varies smoothly, and is typically brighter near the horizon (e.g., Almar et al., 2021); the reflectivity of the surface changes with the angle of incidence of the light, and is maximum at grazing incidence when no light penetrates into water (e.g., Stilwell, 1969). A camera that looks at the reflection of the sky on a flat water surface will see a smooth variation of the pixel intensity, with higher intensities at lower angles of reflection, toward the background of the image. Since light reflects secularly at the water surface, the local angle of inclination (slope) of the surface governs the point of the sky that is reflected at a specific location, and also the angle between the reflection and the surface normal direction. This produces a deformation of the pattern of light intensity that maps between the brightness of the image recorded by the camera at each pixel and the local and instantaneous water surface slope field. If the slope angles are small, the perturbations of the pixel intensities are proportional to the slope variations along the looking direction, and the Fourier spectrum of the pixel intensities is proportional to the surface slope spectrum (Stilwell, 1969). The approach presented here exploits the fact that both the slope spectrum and the spectrum of the surface elevation follow the same dispersion relationship since the slope of a wave moves at the same speed of the wave itself. Once a collection of consecutive images has been orthorectified, that is, once the brightness at each pixel has been assigned to a location on the plane of the water surface, the relation between wavelength and frequency (the dispersion relation) is the same for the image intensity and for the water surface elevation. This allows detection of variations of the water surface dynamics by means of a Fourier analysis of pixel intensity values contained in video images.

3.2. Water Surface Fourier Spectra

In order to estimate the parameters of the dispersion relation, the statistical behavior of the water surface elevation in time and in space needs to be represented. This can be done in terms of a cross-correlation (e.g., Bell, 1999), a cross-spectrum (e.g., Holman et al., 2013), or a 3D Fourier power spectrum (e.g., Dugan et al., 2001) of the water surface elevation. The latter approach is more suited for the complex water surface dynamics of river flows. A 3D discrete Fourier transform decomposes a signal into a combination of waves, each with a certain frequency and wavenumber. The power spectrum indicates how the variance of the signal is distributed among the different

wavenumber and frequency combinations, and its value is expected to be higher where such combinations are close to the theoretical dispersion relations.

The 3D Fourier spectrum of the videos is calculated as follows. First, each pixel intensity value needs to be associated with a unique position in space. This is achieved by means of an image orthorectification algorithm, which uses ground control points with known coordinates to correct the distortions induced by the camera lens and perspective (e.g., Messerli & Grinsted, 2015). The images are projected onto a discretized horizontal plane (x_1, x_2), where $x_1 = \xi\Delta x_1$ and $x_2 = \eta\Delta x_2$ are the horizontal coordinates, $\xi = 0, \ldots, N_1 - 1$, $\eta = 0, \ldots, N_2 - 1$ are integer indices, $\Delta x_1 = L_1/N_1$ and $\Delta x_2 = L_2/N_2$ represent the spatial resolutions, and L_1 and L_2 define the spatial extent of the measurements. Each image represents the surface slope field (see Section 3.1) at a certain time $t = \tau\Delta t$, where $\tau = 0, \ldots, N_t - 1$ is an integer index, $\Delta t = T/N_t = 1/f_s$ is the temporal increment, T is the duration of the recording, and f_s is the sampling rate. $z_{\xi,\eta,\tau}$ is the brightness of the rectified image at location $(\xi\Delta x_1, \eta\Delta x_2)$ at time $\tau\Delta t$. Then, the discrete frequency-wavenumber power spectrum of the image is a 3D array defined as

$$\mathrm{I_{p,q,n}} = \frac{1}{\mathrm{N_1 N_2 N_t}} \left| \sum_{\xi=0}^{\mathrm{N_1}-1} \sum_{\eta=0}^{\mathrm{N_2}-1} \sum_{\tau=0}^{\mathrm{N_t}-1} \mathrm{z_{\xi,\eta,\tau}} \exp\left[-\mathrm{i}2\pi(\mathrm{p}\xi/\mathrm{N_1} + \mathrm{q}\eta/\mathrm{N_2} - \mathrm{n}\tau/\mathrm{N_t})\right] \right|^2, \tag{10}$$

where $p = -N_1/2, \ldots, N_1/2 - 1$ and $q = -N_2/2, \ldots, N_2/2 - 1$ are the integer wavenumber indices in the spatial directions 1 and 2, respectively, and $n = 0, \ldots, N_t$ is the frequency index. The indices p and q correspond to the two components of the wavenumber, $k_1 = p\Delta k_1$, $k_2 = q\Delta k_2$, while the index n is associated with the frequency $\omega = n\Delta\omega$. $\Delta k_1 = 2\pi/L_1$, $\Delta k_2 = 2\pi/L_2$, and $\Delta\omega = 2\pi/T$ identify the spectral resolutions.

3.3. Fitting Procedure

If surface waves follow the dispersion relations presented in Section 2, the spectrum $\mathrm{I}_{p,q,n}$ should be higher for certain combinations of p, q, and n, that satisfy

$$n\Delta\omega \approx \Omega\left(p\Delta k_1, q\Delta k_2, \mathbf{U}_0, d\right), \tag{11}$$

where Ω is one of the dispersion relations of Equation 3 (Ω_A) or Equation 6 (Ω_{GW}). Since Ω depends on $\mathbf{U}_0$ (both Ω_A and Ω_{GW}) and d (only Ω_{GW}), one or both of these parameters can be estimated by "tuning" the dispersion relation until it intersects the largest possible proportion of the higher values of the measured spectrum. According to Serafino et al. (2009), this can be achieved by maximizing the inner product of the measured 3D Fourier spectrum matrix and of a characteristic weighing matrix $\mathrm{M}_{p,q,n}$, with the Normalized Scalar Product (NSP) method. $\mathrm{M}_{p,q,n}$ can be a Gaussian function of the frequency difference, such as (Smeltzer et al., 2019)

$$\mathrm{M}_{p,q,n} = \exp\left\{-[n\Delta\omega - \Omega\left(p\Delta k_1, q\Delta k_2, \mathbf{U}_0, d\right)]^2\right\}. \tag{12}$$

The values of the parameters $\mathbf{U}_0$ and d that provide the best fit between the measured spectra and the theoretical dispersion relation can be estimated by searching for the maximum of the following normalized scalar product:

$$G(\mathbf{U}, d) = \left[\sum_{p,q,n} \mathrm{I}_{p,q,n}\mathrm{M}_{p,q,n}\right] \left[\sum_{p,q,n} \mathrm{I}_{p,q,n} \sum_{p,q,n} \mathrm{M}_{p,q,n}\right]^{-1}. \tag{13}$$

As discussed in Section 2, river surface waves follow different dispersion relations according to their nature and direction of propagation. Therefore, the weighing matrix was modified to account for both types of waves, that is, $\mathrm{M}_{p,q,n}$ was defined as the maximum (at each p, q, n index) of the weighing matrices calculated for Ω_A and Ω_{GW}, respectively,

$$\mathrm{M}_{p,q,n} = \max\left\{e^{-\left[n\Delta\omega - \Omega_{\mathrm{A}}\left(p\Delta k_1, q\Delta k_2, \mathbf{U}_0, d\right)\right]^2}, e^{-\left[n\Delta\omega - \Omega_{\mathrm{GW}}\left(p\Delta k_1, q\Delta k_2, \mathbf{U}_0, d\right)\right]^2}\right\}. \tag{14}$$

This was the same as partitioning the wavenumber-frequency space into two volumes based on the distance from the two surfaces Ω_A and Ω_{GW}, and calculating the weighing based on the closest dispersion relation.

Only the form of Equation 6 with the positive sign was considered. This followed the experimental results of Dolcetti et al. (2016), which showed a poor fit between measurements and the solution with a negative sign.

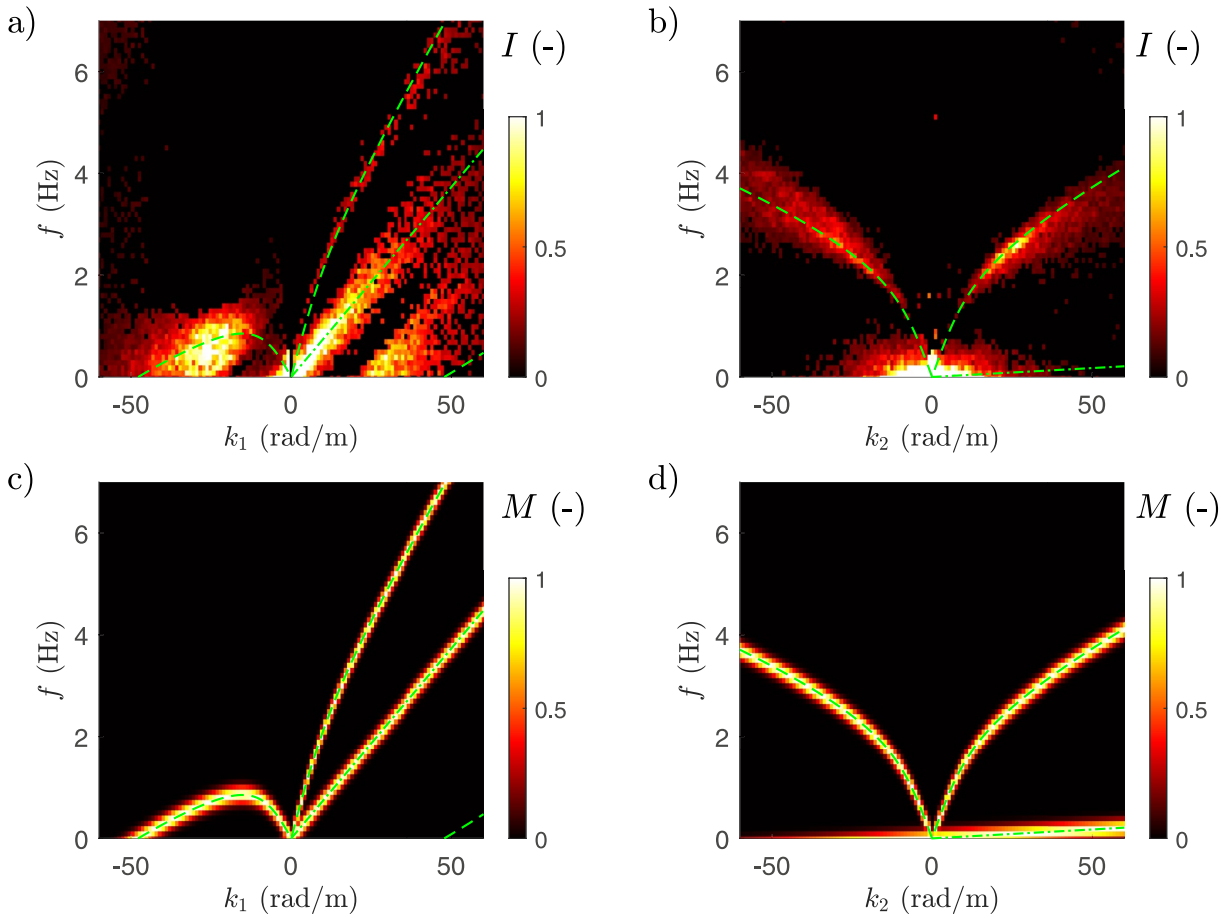

Figure 3. Example of spectra fitting procedure. (a and b), Normalized measured frequency-wavenumber power spectra of a sequence of images of the water surface, $I_{p,q,n}$. (c and d), weighing matrix $M_{p,q,n}$, after fitting. (a and c), cross-sections of the 3D power spectra in the streamwise direction, that is, for $k = k_1$. (b and d), cross-sections of the 3D power spectra in the transverse direction, that is, for $k = k_2$. The green lines show the theoretical dispersion relations calculated for the best-fit parameters values. (Dashed), Ω_{GW}. (Dashed-dotted), Ω_A. The example is based on flow condition S04 (see Table 1).

The solution with the negative sign represents GC waves that attempt to propagate against the flow, but with a relatively low speed, so that they are swept downstream by the mean flow. The failure to represent these waves accurately could be due to the presence of a critical layer, that is, a plane where the mean flow velocity matches the speed of the water waves, enabling a resonant exchange of energy between flow and water surface which violates the assumptions of linearity and stationarity upon which Equation 6 is based (Zakharov & Shrira, 1990). Even with other models of vertical profile of streamwise velocity, these interactions are difficult to study, because models with nonconstant vorticity have a singularity at the critical layer, which does not appear to have been addressed in previous studies (e.g., Fenton, 1973).

Examples of a measured Fourier spectrum and of the weighing matrix $M_{p,q,n}$ are shown in Figures 3a and 3b, and in Figures 3c and 3d, respectively. The problem of maximizing G was solved by means of a Self-Adaptive Differential Evolution (SADE) algorithm (Qin & Suganthan, 2005). This algorithm was found to be more robust and less dependent on the choice of the initial conditions compared to preliminary attempts with alternative methods (e.g., least squares, simplex). Details of the data preprocessing and optimization procedure are provided in Appendix A.

4. Sensitivity and Uncertainties

This section includes a discussion of the factors that can affect the estimation of the surface velocity, depth, and discharge.

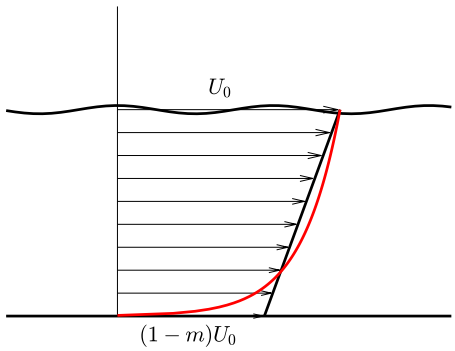

Figure 4. Schematic of the linear vertical profile of the streamwise velocity (black), compared to a power-function profile (red). The linear profile has $m = 0.34$. The power-function profile has $\eta = 0.2048$. Both profiles have a velocity index $\alpha = 0.83$.

4.1. Idealization of the Velocity Profile

The linear velocity profile described in Equation 5 was used to allow a practical explicit solution of the dispersion equation and is argued in this context to be a pragmatic approximation of the typical vertical profile of streamwise velocity in a river reach. Figure 4 shows a comparison of the linear profile and a power function profile $U(z) \propto z^{\eta}$, where η was chosen in order to yield the same depth-averaged to surface velocity ratio for both profiles. The accuracy of the linear profile model is less for the longer water waves that interact with a more strongly sheared flow closer to the bed. These waves tend to be dominant at higher Froude number flows. For instance, the difference between the values of the characteristic wavenumber k_0 calculated for the linear and for the power-function velocity profile (Fenton, 1973), is less than 1% for Froude numbers lower than 0.5, but it can be as high at 20% for Froude numbers close to one (Dolcetti & García Nava, 2019a). Unfortunately, approximations of the velocity profile beyond first order yield dispersion relations in an implicit form, that can only be solved numerically, which in this application would require very significant computational resources. Considering a typical set of 300×300 wavenumber values, 20 initial populations for the genetic algorithm, and around 100 iterations before convergence, the dispersion relation needed to be calculated 1.8×10^8 times on average, for each run of the optimization algorithm. A single run of the analysis assuming a power-function profile was performed using the data set indicated as S11, which had an intermediate water depth and Froude number $\mathsf{F} = 0.53$ (see Table 1). Compared to the linear profile solution, this yielded a difference of 1.2% for the speed and of 7.4% for the depth. However, the analysis time required was more than 20 times longer than the time taken by the linear profile solution. In the context of using a few minutes of images to monitor the flow discharges during a flood event, such a slow analysis would be impractical.

4.2. Estimation of the Velocity Index

Predicting the flow rate requires the estimation of two parameters. The first one is the velocity gradient m that defines the shape of the velocity profile and affects the relationship between the measured wave frequency and the unknown water depth and surface velocity through Equation 7. In principle, m could be treated like an additional unknown parameter and estimated in the same way as U_0 and d. Unfortunately, our attempts to estimate all parameters at the same time based on the measured videos and without additional constraints gave uncertain results, which suggested a nonuniqueness of the inverse problem. Therefore, the value of m had to be assumed a priori. The second parameter is the velocity index α, that is, the ratio between the depth-averaged velocity and the surface velocity. α allows the discharge to be calculated based on the estimated surface velocity, following Equation 2. Although it is required by most noncontact measurement methods, the estimation of α is often the largest source of uncertainty for the discharge (Hauet et al., 2018; Welber et al., 2016). According to Hauet et al. (2018), unless the possible range of variation of the velocity index can be constrained based on additional information on the site, a minimum uncertainty of $\pm 15\%$ at 90% confidence levels should be assumed for α, and therefore for the discharge determined with noncontact methods.

In principle, m and α can be chosen independently. Since both parameters are related to the shape of the vertical profile of the streamwise velocity, it was decided to link them, expressing the velocity gradient m as a function of α. In fact, the ratio between depth-averaged velocity and surface velocity for the linear velocity profile of Equation 5 is

$$\alpha = \frac{1}{dU_0}\int_0^d U(z)\mathrm{d}z = 1 - \frac{m}{2}. \tag{15}$$

Therefore, it was assumed that m could be calculated as a function of α as

$$m = 2(1-\alpha). \tag{16}$$

Then, all flow parameters (water depth, surface velocity, and discharge) could be estimated by assuming a single parameter α.

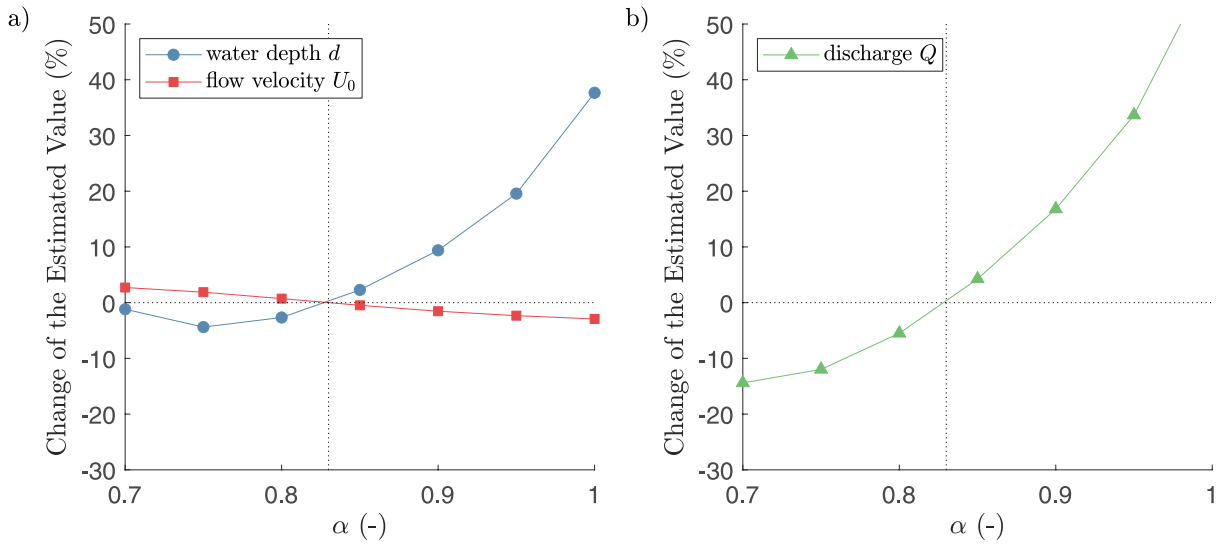

Figure 5. Relative variation of the estimated flow parameters as a function of the assumed velocity index α. The relative changes are with respect to the estimations obtained with $\alpha = 0.83$. Variations of the estimated depth and surface velocity (a) are due to the dependence of the velocity gradient m on α through Equation 16. Variations of the discharge (b) are due also to the direct dependence on α according to Equation 2.

The choice of the value of α was based on existing guidance for noncontact velocimetry (Hauet et al., 2018). Data collected in a large number of small rivers by Hauet et al. (2018) revealed typical values of α between 0.7 and 0.95, with an average of 0.83, and with slightly higher values for deeper flows. Therefore, here α was set to 0.83, and consequently $m = 0.34$ (Figure 4). An attempt to link the value of α to the depth by means of existing relations (Le Coz et al., 2010; Welber et al., 2016) was carried out but the results did not show a significant improvement.

Figure 5 shows an example of how the estimates of U_0 d and Q change with a change of α. The example is based on the analysis of actual data recorded in flow condition S11, and performed assuming different values of α between 0.7 and 1 (which correspond to $0.6 \geq m \geq 0$). The reference for the change of the estimated parameters is $\alpha = 0.83$ ($m = 0.34$). The variation of U_0 and d is due to the change of m. The effect on U_0 is relatively small, with variations <3% for α between 0.7 and 1. The sensitivity of d is larger, with variations between −4.4% and 37.7%, with the largest values when $\alpha > 0.9$. Since the discharge depends on both U_0 and d as well as on α, its sensitivity to the choice of α is larger. For the example shown in Figure 5, a ± 10% uncertainty of α yields a ± 1.9% uncertainty of U_0, a ± 9.4% uncertainty of d, and a ± 16.8% uncertainty of Q.

4.3. Sensitivity to Flow Parameters

As shown in Figure 2, flow speed variations have a much larger impact on the wave frequency than depth variations, at least in conditions of typical shallow river flows. Here, the sensitivity to speed and depth variations is quantified in terms of the nondimensionalized partial derivatives of Ω_{GW}, and expressed as a function of the nondimensional wavenumber kd, of the Froude number $\mathsf{F} = U_0/\sqrt{gd}$, of the Bond number B, and of the velocity gradient m. The resulting equations obtained by differentiating Equation 6 are complicated in their complete form, therefore they are presented in Appendix B. In the small-shear gravity-wave limit, $m \to 0$ and $\mathsf{B} \to \infty$, the nondimensional sensitivity factors (indicated as $\xi_{(.)}$, where (.) is the parameter being considered) have a simpler form, as follows:

$$\xi_{U_0} = \sqrt{\frac{d}{g}} U_0 \left(\frac{\partial \Omega_{GW}}{\partial U_0} \right) \approx (\mathbf{k}d) \cdot \mathbf{F} \tag{17}$$

$$\xi_d = \sqrt{\frac{d^3}{g}} \left(\frac{\partial \Omega_{GW}}{\partial d} \right) \approx \frac{kd}{2\cosh^2(kd)} \sqrt{\frac{kd}{\tanh(kd)}} \tag{18}$$

Figure 6 illustrates the behavior of ξ_{U_0} and ξ_d as a function of F and kd. The factors have been calculated for $\mathsf{B} \to \infty$ and $m = 0.34$, but a qualitatively similar behavior could be observed for different values of B and m.

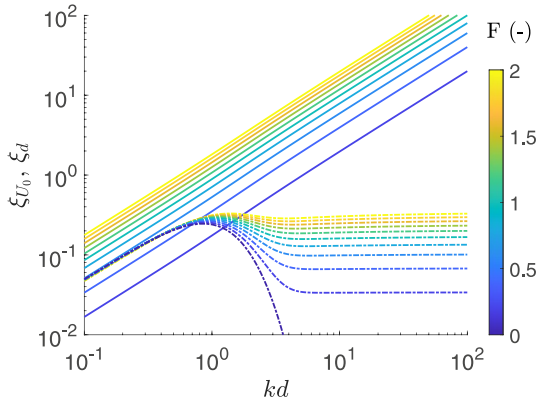

Figure 6. Nondimensional sensitivity parameters, which indicate the sensitivity of the waves dispersion relation with respect to (solid) speed variations, ξ_{U_0}, and (dashed) depth variations, ξ_d. Data are expressed as a function of the nondimensional wavenumber kd and Froude number F. An example calculated with $m = 0.34$, in the $\mathsf{B} \to \infty$ gravity waves limit.

The sensitivity to flow velocity variations, ξ_{U_0}, increases linearly with F and with kd, meaning that the measurements are expected to be more accurate when the surface waves are relatively short. The inner product in Equation 17 means that the sensitivity is maximum for waves that propagate parallel to the flow direction, while it would be impossible to estimate the flow velocity if all measured waves were propagating perpendicularly to the flow, since in this case $\mathbf{k} \cdot \mathbf{F} = 0$, and Ω_A and Ω_{GW} would both be independent by U_0. The sensitivity to depth variations, ξ_d, increases almost linearly with kd when $kd < 1$, it reaches a maximum when $kd \approx 1$, then it stabilizes to a lower constant value, which increases with F. This indicates that estimates of the flow depth are expected to be more accurate when the surface waves have a wavelength $\lambda \sim 2\pi d$. If $m = 0$, then there is no Froude number influence (see Equation 18), and ξ_d tends to 0 at large kd.

5. Data Collection

5.1. Measurement Sites

Validation was performed on data from two sites: the River Sheaf, in Sheffield, United Kingdom (Latitude: 53.373056° Longitude: −1.463913° (WGS 84)), and the River Calder, in Todmorden, United Kingdom (Latitude: 53.716198° Longitude: −2.097028°). These sites were chosen because they were located upstream of high quality conventional flow rate measurement gauging stations that could provide a direct comparison with the proposed methodology. Both rivers had an approximately trapezoidal channel shape (homogeneous flow, velocity index within typical range). The channel flow width was constrained by fixed walls, but the channel bed was composed of natural gravels that were potentially mobile.

The Sheaf is one of the main tributaries of the River Don with a catchment area of 49.1 km^2 (at the gauging station). The lower part of the catchment is highly urbanized. The reach was effectively straight with a channel width of around 9.25 m, a bed slope of approximately 0.011, and a "stable" coarse gravel bed. The measurement area was situated 25 m upstream of a river gauging station operated by the UK Environment Agency, where the stage was monitored continuously by means of a calibrated pressure transducer. Measurements of the water depth at the same time of the videos were obtained indirectly, converting the stage data by means of a linear stage-to-depth relation. This relation was calibrated with direct measurements of the water depth performed in two separate occasions at 25 locations distributed evenly across the measurement area, and with indirect estimates of the water level relative to a fixed reference visible in each video. All data are presented in terms of water depth. Gauging surveys had been performed manually by the UK Environment Agency in 87 occasions between 1993 and 2019, with a standard propeller meter (1993–2011), and with an acoustic Doppler current profiler (ADCP) (since 2011). The historical survey data were used to produce an empirical depth-discharge curve, which was used to compare with the estimates obtained with the proposed water surface wave method. The mean annual discharge at the monitoring station is 0.583 m^3/s (period of record: 1981–2018), the 5th flow percentile is 1.925 m^3/s and the 95th flow percentile is 0.083 m^3/s (National River Flow Archive, 2020). The measurements in this study covered a range of discharge between 0.29 m^3/s and 5.14 m^3/s, corresponding to a width/depth ratio between 132 and 19, respectively.

The Calder is a predominantly urban river. The river monitoring station is located within the town of Todmorden, with a catchment area of 18.2 km^2. Here, the 5 m wide channel has a stable coarse gravel bed and has brick walls extending over 2.5 m in height. The reach is broadly straight with a 19° curve on the approach to the imaged section where the bed slope is approximately 0.013. The measurement area was situated 10 m upstream of a river gauging station operated by the UK Environment Agency, where the stage was monitored continuously by means of a calibrated pressure transducer. The discharge was measured every 15 min by means of a bed-mounted ADCP (SonTek-IQ). The width/depth ratio varied between 7 and 26 across all measurements.

5.2. Video Acquisition and Processing

The videos of the River Sheaf were recorded using a camera (Hikvision DS-2CD2T42WD-I8 6 mm IP), operating at 20 fps at a resolution of 1,920×1,080 pixels. The camera was installed on the left bank channel wall,

approximately 4.5 m above the river bed, looking upstream with an angle of approximately 30° from the horizontal. The videos had a duration of 5 min. They were recorded daily at 1 p.m., and sent automatically to an online repository, from which they were accessed and analyzed. The analysis was based on 17 time series of images recorded between January 2019 and February 2020, which were selected in order to provide a range of flow conditions.

The videos of the River Calder were recorded using the same model of camera, but at a higher resolution of 2,688 × 1,520 pixels. The camera was installed on the left bank channel wall, approximately 3.9 m above the river bed, looking upstream with an angle of approximately 16° from the horizontal. The videos used for the analysis were taken between 6 and 13 October 2020, during a period that saw three flow rate peaks. Each video had a duration of 30 s, and were recorded every 15 min. These videos experienced compression and frame rate issues resulting in the loss of a small number of frames. The analysis covered 12 time image series, which were selected based on the time of day (measurements distributed at different times, avoiding night time), weather conditions (with and without rain), number of skipped frames (videos with more than 2% of skipped frames were excluded), and flow conditions (to provide a range of conditions).

The images from both sites were rectified to remove lens and geometric distortions. Intrinsic parameters of the camera lens (i.e., radial and tangential distortion coefficients, camera focal length, and image center parameters), were determined using a 841 × 1,189 mm checkerboard pattern and the Camera Calibrator App within Matlab 2017b. External parameters of the camera location were surveyed, while the view direction was optimized using surveyed ground control points within the camera field-of-view. Changes in water surface level over time were accounted for during the orthorectification process (Messerli & Grinsted, 2015). The rectified image was defined onto a spatial grid with size 0.02 × 0.02 m for the River Sheaf, and 0.01 × 0.01 m for the River Calder.

In order for the estimations of the flow parameters to be accurate, both short and long waves must be measurable with a reasonable accuracy. Therefore, the camera must have both a suitable resolution and a large field of view. The flow velocity estimates are based mainly on the dynamics of short waves (see Figure 6), therefore their accuracy is mostly affected by the image resolution (pixel size) and frame rate (Piotrowski & Dugan, 2002). The spectral resolution, instead, represents the smallest variation of the frequency and/or of the wavenumber that can be detected, which is inversely proportional to the temporal and spatial extent of the measurements, $\Delta\omega = 2\pi/T$ and $\Delta k = 2\pi/L$. The spectral resolution should not be large compared to the sensitivity of the dispersion relation to depth and velocity variations (ξ_d and ξ_{U_0}), otherwise these variations cannot be detected (Piotrowski & Dugan, 2002; Smeltzer et al., 2019). This imposes some limits on the minimum size of the images and on the minimum recording duration, that is,

$$kL \gg 1, \qquad \omega T \gg 1, \tag{19}$$

where k and ω are some representative wavenumber and frequency of the water surface fluctuations, respectively. Based on Figure 6, the sensitivity to depth variations is highest for $kd \sim 1$, therefore the size of the image must be substantially larger than the water depth in order to obtain a reliable estimate of the flow depth.

In order to obtain a sufficient spectral resolution for a range of flow conditions the analysis was applied to a window size comparable to the width of each river. For the River Sheaf, the window was square with size of 6 × 6 m, while the characteristic wavelength λ_0 (Equation 8) varied between 0.06 m (0.01 L, condition S01) and 1.3 m (0.2 L, condition S16). The River Calder appeared to be dominated by longer waves, and had a smaller width. The size of the window had to be limited to 4 × 3 m, which corresponded to a spectral resolution of 1.6 × 2.1 rad/m. The characteristic wavelength was estimated between 0.5 m (0.13 L, condition C01) and 3.1 m (0.8 L, condition C12), according to Equation 8. For both rivers, the videos were split into segments of 10 s duration, and the spectra were averaged across the different segments. For the River Sheaf, the spectrum was the average of 29 independent measurements. For the River Calder, due to the short duration of the videos, it was only possible to obtain 10 segments, with 80% overlap.

5.3. Water Surface Appearance and Fourier Spectra

An example of a single video snapshot on the River Sheaf in flow condition S16 (see Table 1) is shown in Figure 7a. Figure 7b shows the corresponding rectified image, while Figure 7c shows a rectified snapshot obtained for a different flow condition (S08). The red square in Figures 7a and 7b shows the border of the area that was used for analysis. Water surface deformations are clearly visible in the images, and their characteristic

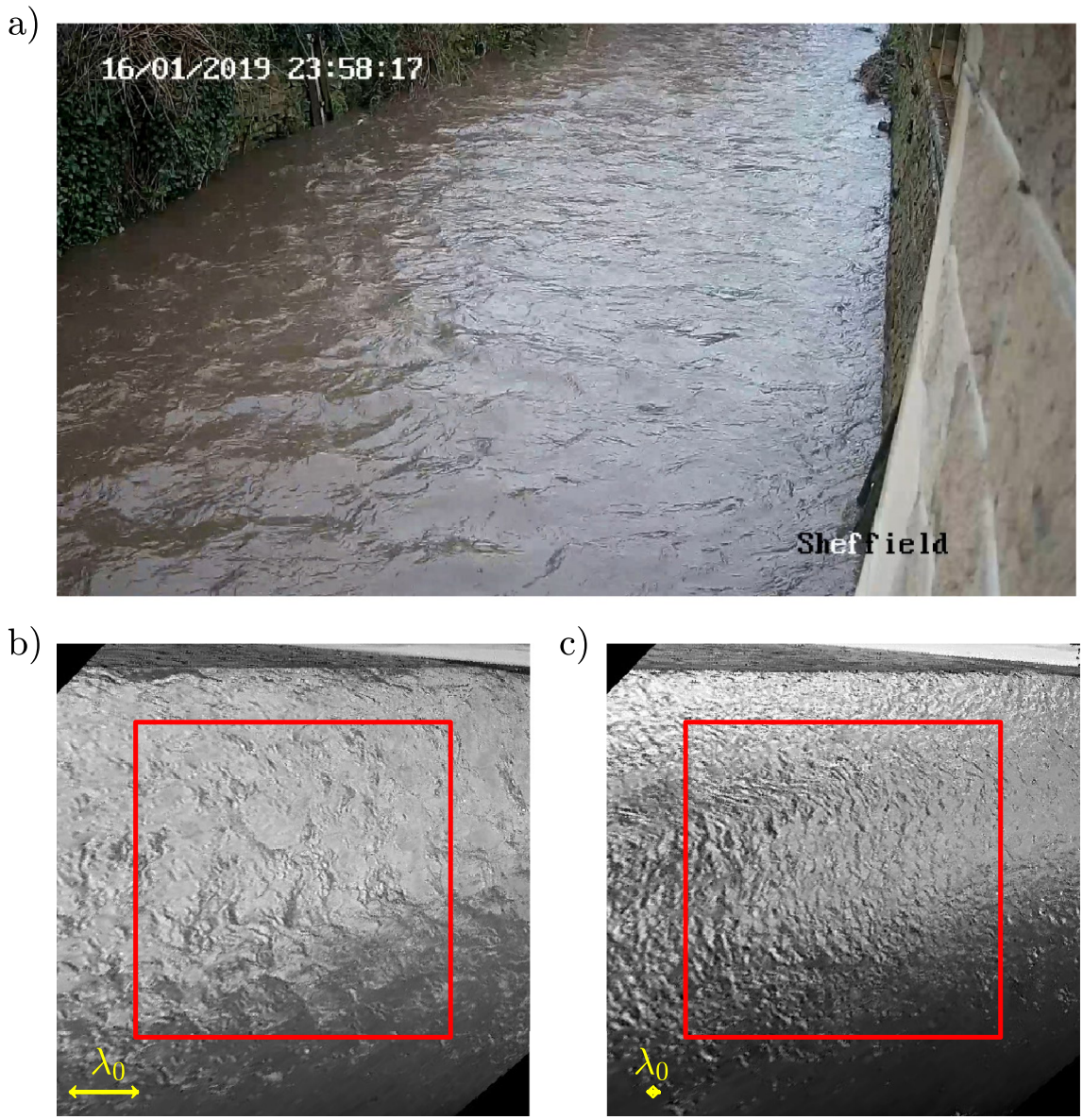

Figure 7. (a) A snapshot of a video of the River Sheaf (flow condition S16). (b and c) Examples of orthorectified images recorded in flow condition (b) S16 and (c) S08. The red square indicates the borders of the area used for the analysis. λ_0 is the characteristic wavelength estimated by Equation 8.

scales seem to be different for the two flow conditions (shorter in Figure 7c). According to observations by Dolcetti et al. (2016) in a laboratory flume, the dominant horizontal scale of the water surface in shallow flows is represented by λ_0, obtained from Equation 8. The scale λ_0 has been shown in Figures 7b and 7c for both flow conditions, as a reference.

Examples of the measured average frequency-wavenumber spectra $I_{p,q,n}$ calculated for flow condition S11 are shown in Figure 8. Each plot in Figures 8b–8d is a different section through the 3D spectrum, as illustrated in Figure 8a. Figure 8b shows the transverse spectrum ($k_1 = 0$) at all frequencies, Figure 8c shows the streamwise spectrum ($k_2 = 0$), while Figure 8d shows both components of the wavenumber at a constant frequency of $\omega = k_0 U_0 = 11.5$ rad/s. The green lines in Figures 8b–8d, indicate the theoretical dispersion relations of GC waves and of turbulence-generated structures. They have been calculated based on the values of the flow parameters estimated with the procedure described in Section 3. Both types of water surface waves are clearly visible.

Figure 9 shows some examples of images recorded on the River Calder, before rectification (Figure 9a, for flow conditions C08) and after rectification (Figures 9b and 9c, for flow conditions C08 and C02). Compared to the

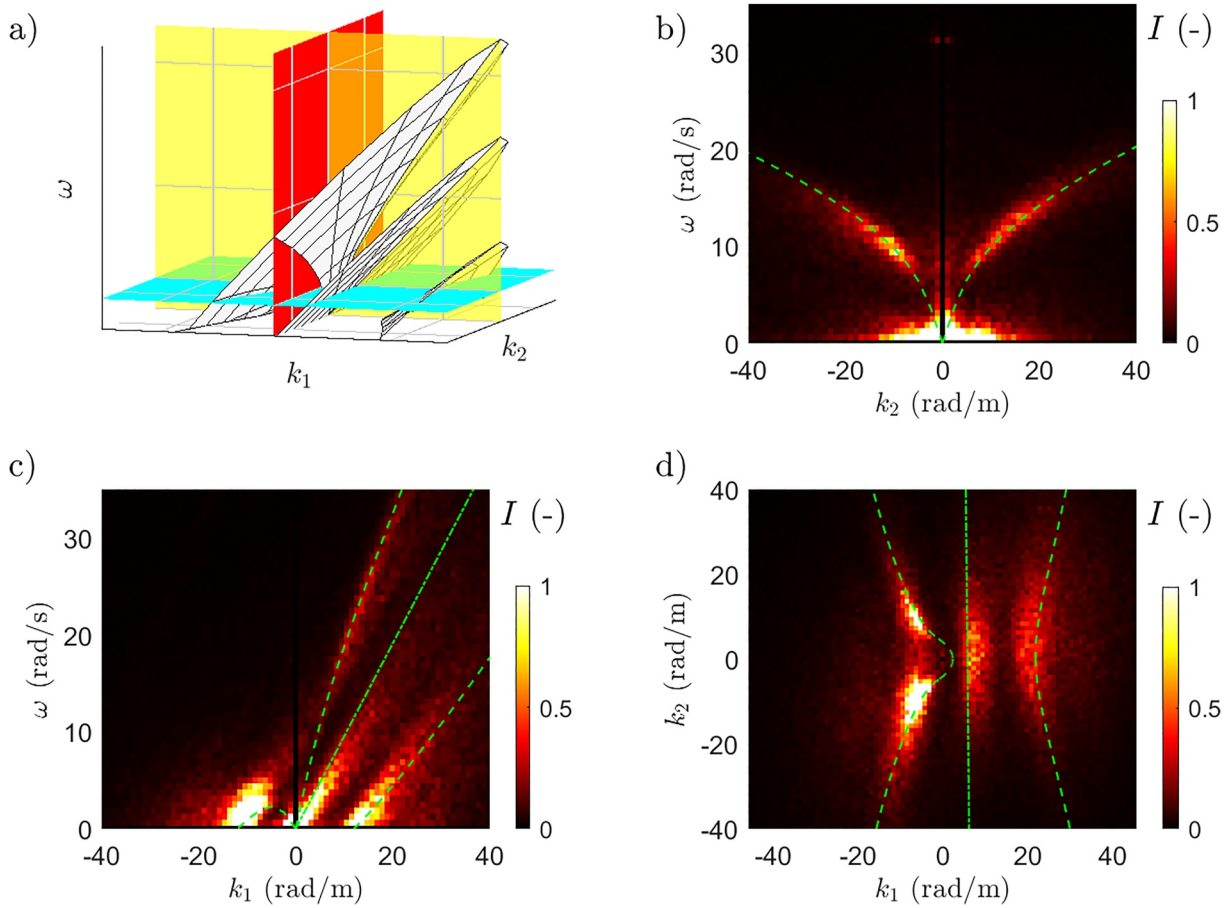

Figure 8. Normalized measured frequency-wavenumber spectra of a video of the River Sheaf (flow condition S11). (a) Schematic of the dispersion relation of gravity-capillary (GC) waves and turbulence-generated surface deformations. The colored planes indicate sections of the 3D spectrum shown in (b and c, and d). (b) Spectrum of transverse waves [$k_1 = 0$ - Red plane in (a)]; (c) spectrum of waves with the crest perpendicular to the flow [$k_2 = 0$ - yellow plane in (a)]; and (d), section at constant frequency $\omega = k_0 U_0$ (blue plane in (a)). (green dashed lines): dispersion relation of GC waves, Equation 6. (green dashed-dotted lines): dispersion relation of turbulence-generated deformations, Equation 3.

River Sheaf, the characteristic wavelength of the water surface fluctuations seems larger relative to the river width. An example of the frequency-wavenumber spectrum recorded on the River Calder for flow condition C08 is shown in Figure 10. Compared to the spectra of the River Sheaf shown in Figure 8, the spectra in Figure 10 appear noisier. This was due in part to the shorter duration of the videos of the River Calder, with a small number of averages, and more limited spectral resolution due to the longer waves. The presence of both types of surface waves can be observed by comparison with the theoretical dispersion relations in Figure 10.

The actual characteristic scales of the water surface waves were quantified in terms of the spatial Fourier spectra of the image intensities. These were obtained by integrating the frequency-wavenumber spectra along the frequency axis in order to obtain the directional 2D wavenumber spectra, transforming these in polar coordinates, and then averaging along the polar angle. The analysis was applied only to the conditions with $\lambda_0 < L_{min}/2$, where L_{min} is the smaller dimension of the rectangular window, since for longer waves the transform to polar coordinates was deemed unreliable at small k. The resulting omnidirectional spectra represent the power spectral density of the image intensity as a function of the wavenumber modulus k, and are shown in Figure 11 for the data collected in both rivers.

For both data sets, the spectra appear to have a peak at approximately $k = k_0$, which demonstrates that the dominant scale is represented effectively by Equation 8. There is a sharp cut-off at lower wavenumbers, indicating that λ_0 is also the longest wavelength at the water surface. Another cut-off is found at higher wavenumbers, corresponding to a wavelength of approximately 50 mm, which aligns with the image spatial resolution. In the

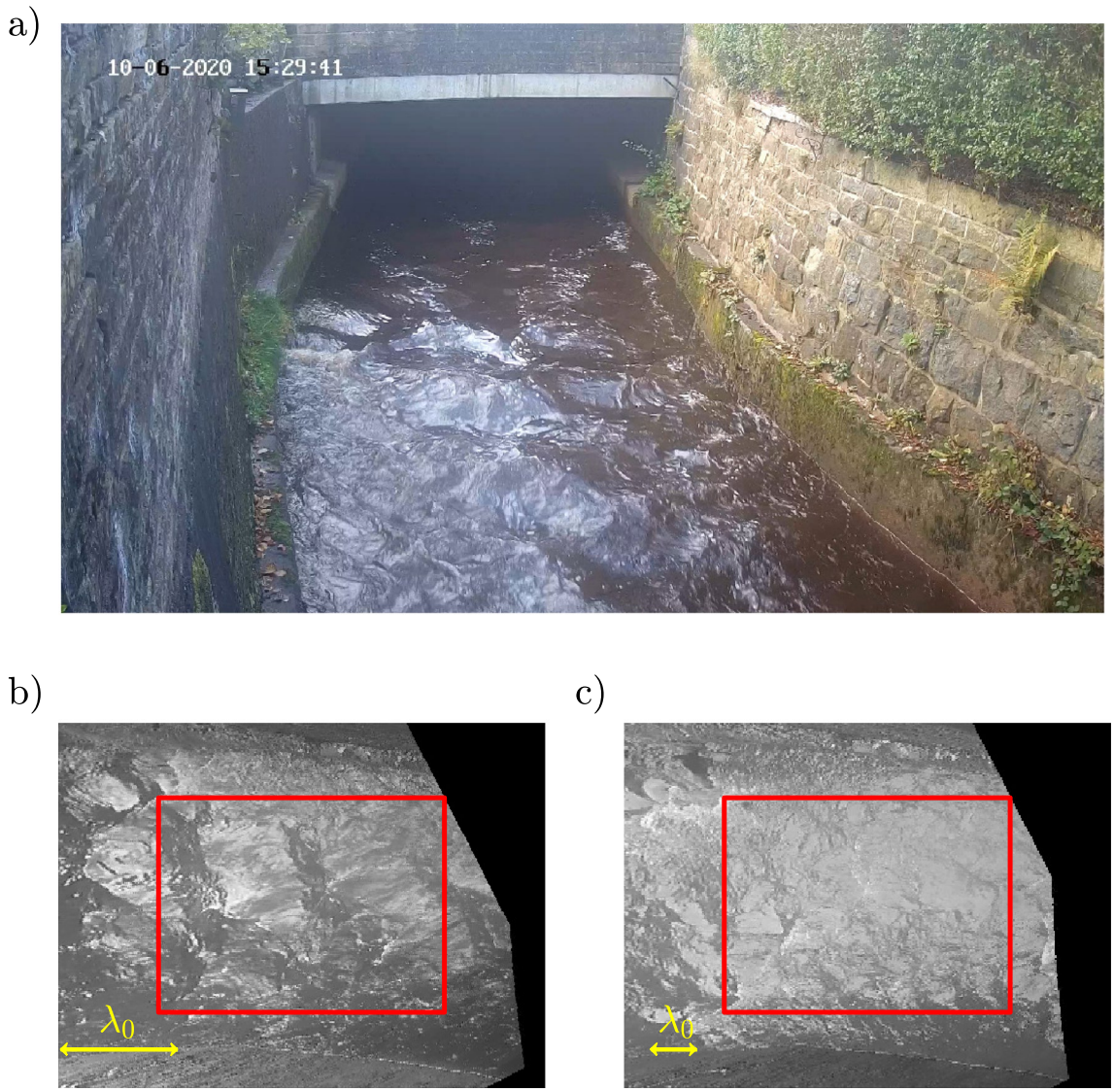

Figure 9. (a) A snapshot of a video of the River Calder (flow condition C08). (b and c) Examples of orthorectified images recorded in flow condition (b) C08 and (c) C02. The red square indicates the borders of the area used for the analysis. λ_0 is the characteristic wavelength estimated by Equation 8.

intermediate range of wavenumbers, the spectra decay following roughly a power function k^{-c}, with the exponent c that increases with the Froude number. A line proportional to $k^{-1/4}$ is shown for reference in Figure 11.

5.4. Measurement Uncertainties

As discussed in Section 4, the measurement uncertainty is governed by multiple factors. An attempt was made to estimate the uncertainty that relates to the measurement resolution. This was done a posteriori, with the aid of a numerical model that created synthetic images of the water surface, with a spectrum similar to the ones observed in Figure 11. The synthetic videos were built by a Fourier synthesis method (e.g., Dolcetti & Krynkin, 2017) applied to a simplified spectrum that followed $\sim k^{-1/4}$, with cut-offs at the wavenumbers k_0 and $2\pi/0.05$ rad/m. The wavenumber spectrum was transformed into a frequency-wavenumber spectrum by means of the dispersion relations (Equations 3 and 6), using the estimated values of the flow parameters d and U_0 (hence, a posteriori). Sequences of synthetic images were constructed by multiplying the theoretical spectrum at each wavenumber-frequency combination by a set of complex factors drawn from a normal distribution, and then applying an inverse Fourier transform in space and in time to the randomized spectrum. This procedure ensures that the average spectrum

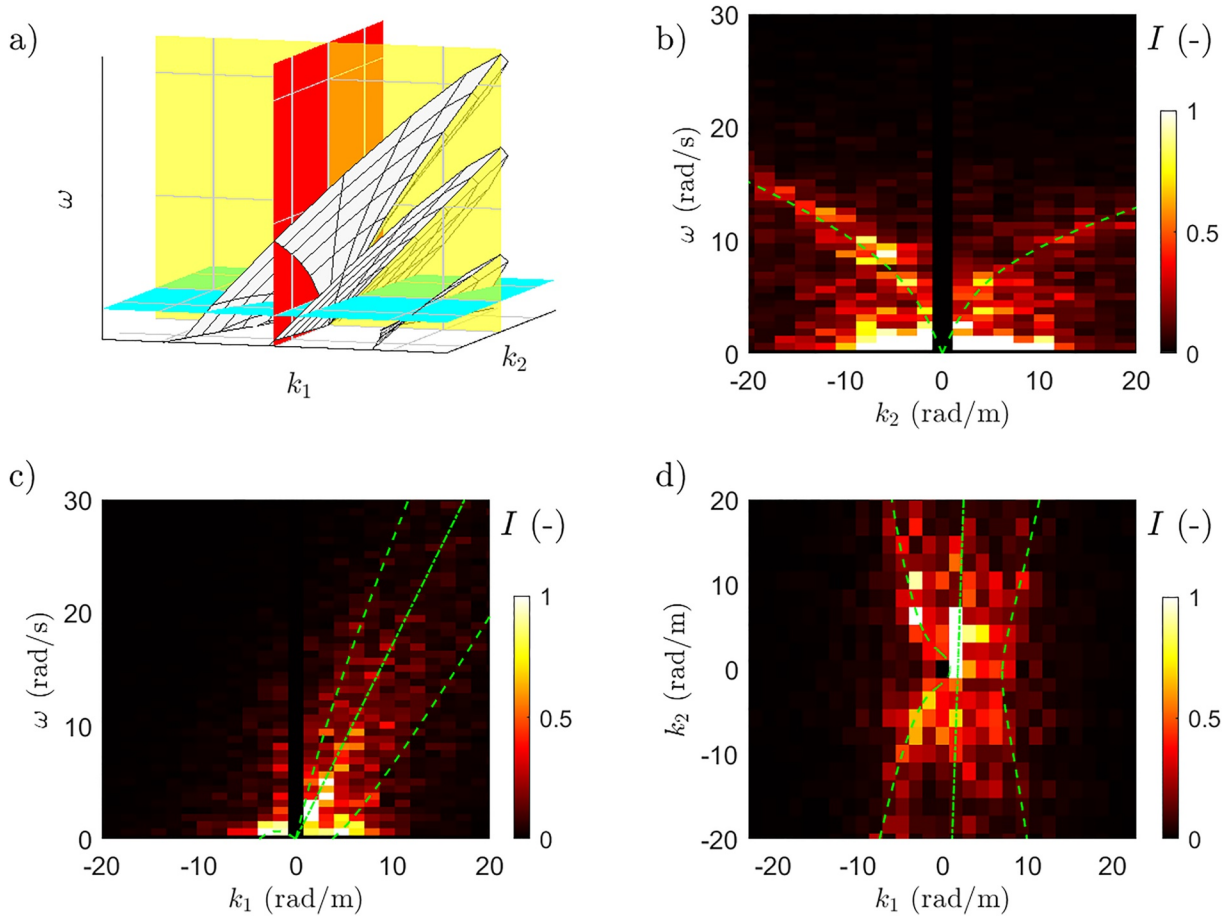

Figure 10. Normalized measured frequency-wavenumber spectra of a video of the River Calder (flow condition C08). (a) Schematic of the dispersion relation of gravity-capillary (GC) waves and turbulence-generated surface deformations. The colored planes indicate sections of the 3D spectrum shown in (b, c, and d). (b), spectrum of transverse waves ($k_1 = 0$ - red plane in (a)); (c), spectrum of waves with the crest perpendicular to the flow ($k_2 = 0$ - yellow plane in (a)); and (d), section at constant frequency $\omega = k_0 U_0$ (blue plane in (a)). (Green dashed lines): Dispersion relation of GC waves, Equation 6. (green dashed-dotted lines): dispersion relation of turbulence-generated deformations, Equation 3.

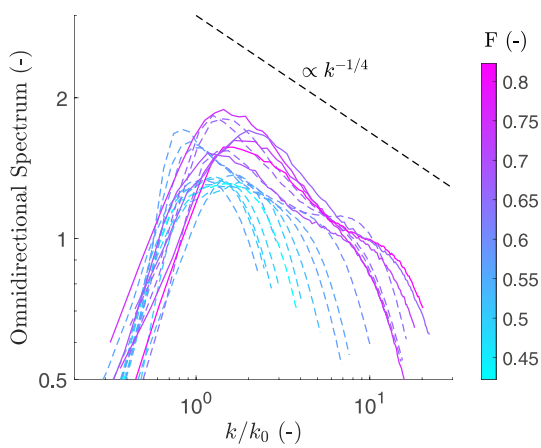

Figure 11. Omnidirectional spatial spectra of the image intensity. (dashed), River Sheaf and (solid), River Calder. k_0 is the characteristic wavenumber according to Equation 8. Only the flow conditions with $\lambda_0 < L_{min}/2$ are shown.

of the synthetic surfaces coincides with the theoretical spectrum. The synthetic data were sampled spatially and temporally like the real data, therefore they had the same spatial, temporal, and spectral resolution.

The synthetic data followed exactly the theoretical dispersion relations calculated for the input flow parameters. However, because of the uncertainties, the flow parameters estimated with the analysis differed from the input values. For each flow condition, 5 synthetic videos were created and analyzed, and the uncertainties were quantified in terms of a root-mean-squared deviation from the input values of the flow parameters. The deviations calculated in this way represent only the effects of limited measurement resolution, and of the limited sensitivity of the surface dynamics to changes in flow parameters. They represent a lower boundary of the actual measurement uncertainties.

The uncertainties estimated based on synthetic data varied greatly with the flow conditions, because of the different characteristic surface wavelength and period. The values are presented as dimensional uncertainties of the estimated parameters in Tables 1 and 2 for the two data sets. For the River Sheaf, the rms-deviation based on synthetic data for both d and Q varied between 2.2% (flow condition S05, with $k_0 L = 204$) and 13.5% (flow conditions S15,

S16, and S17, with $k_0L \approx 30$). The rms-deviation of U_0 was less than 0.3% for all flow conditions (not shown in Table 1).

The flow conditions at the River Calder were relatively deeper, the window size to wavelength ratio was smaller, and therefore the uncertainty due to the limited spectral resolution was larger. For one measurement (06 October 2020, 12:00), the algorithm failed to find a maximum of the normalized scalar product within the search range, resulting in a very large uncertainty of the depth, ±90%. This flow condition was discarded from further analysis. For the remaining flow conditions, the rms-deviations of d and Q varied between 2.4% (condition C01, $k_0L = 49$) and 24.7% (condition C12, $k_0L = 8$), while the uncertainties of U_0 were always less than 0.5%.

6. Results

The measured and estimated water depths and flow rates are listed in Tables 1 and 2, for each analyzed video of the River Sheaf and River Calder, respectively. The uncertainties in the table were calculated a posteriori from synthetic data, as explained in Section 5.4. The relative differences between measured and estimated depth and discharge are indicated as err_d and err_Q, respectively. The comparison between measured and estimated water depth and discharge is also illustrated in Figures 12 and 13, respectively.

For the measurements of the River Sheaf, the difference between measured and estimated depth varied between 0.5% (measurements S08, S12, and S13) and 34% (S05), with a root-mean-squared average across measurements of 16.3%. Larger deviations were observed at the deeper and at the shallower flows. For the River Calder, the relative difference between measured and estimated water depth was found to vary between 2% (measurement C12) and 38% (C05), with most values (except C08 and C05) below 15%, and with an rms difference across all measurements of 15.5%.

The difference between measured and estimated flow rates for the River Sheaf (Figure 13a) varied between 0.4% (S08) and 52.6% (S15), with a root-mean-squared average across measurements of 27.8%. In comparison, the expected rms uncertainty estimated with synthetic data was 6% for both d and Q. The rms difference between the gauged discharges and the ones predicted by the fitted rating curve was 9%. For the River Calder, the difference

Table 1
Measured and Estimated Flow Parameters, River Sheaf

Measurement		Measured		Estimated		Error				
Name	Date	d_{meas} (m)	Q_{meas} (m^3/s)	d_{est} (m)	Q_{est} (m^3/s)	err_d (%)	err_Q (%)	F_{est} (−)	k_0d (−)	k_0L (−)
S01	02 February 2019	0.07	0.29	0.07 ± 0.00	0.18 ± 0.01	4.1	−37.9	0.38	7.7	661
S02	24 January 2019	0.07	0.29	0.07 ± 0.00	0.18 ± 0.01	−4.2	−38.3	0.41	6.6	560
S03	11 January 2020	0.12	0.50	0.14 ± 0.00	0.67 ± 0.02	15.2	33.8	0.59	3.2	161
S04	22 January 2019	0.12	0.52	0.10 ± 0.00	0.35 ± 0.01	−20.2	−32.6	0.43	5.9	289
S05	17 June 2019	0.15	0.68	0.10 ± 0.00	0.42 ± 0.01	−33.9	−37.6	0.46	5.1	204
S06	21 March 2019	0.16	0.75	0.13 ± 0.00	0.57 ± 0.01	−19.8	−23.2	0.46	5.0	189
S07	08 March 2019	0.17	0.84	0.15 ± 0.00	0.68 ± 0.02	−15.8	−18.6	0.47	5.0	171
S08	10 February 2019	0.18	0.87	0.18 ± 0.01	0.87 ± 0.04	−0.5	0.4	0.49	4.6	155
S09	06 March 2019	0.22	1.20	0.23 ± 0.01	1.30 ± 0.03	3.3	8.5	0.51	4.2	114
S10	03 October 2019	0.22	1.24	0.30 ± 0.01	1.66 ± 0.07	33.2	33.1	0.49	4.6	122
S11	08 February 2019	0.26	1.59	0.27 ± 0.01	1.75 ± 0.06	3.5	9.9	0.53	3.9	90
S12	07 February 2019	0.31	2.12	0.30 ± 0.01	2.29 ± 0.07	−0.5	8.1	0.57	3.5	68
S13	12 June 2019	0.34	2.60	0.34 ± 0.02	2.72 ± 0.12	0.4	4.7	0.56	3.5	61
S14	16 March 2019	0.37	3.05	0.41 ± 0.04	3.75 ± 0.34	9.6	23.0	0.63	2.9	46
S15	20 February 2020	0.42	3.82	0.51 ± 0.04	5.83 ± 0.48	22.3	52.6	0.73	2.1	31
S16	12 March 2019	0.49	5.14	0.57 ± 0.08	6.67 ± 0.90	16.8	29.8	0.70	2.3	29
S17	14 March 2019	0.49	5.14	0.51 ± 0.05	5.88 ± 0.58	5.8	14.4	0.68	2.4	30

Table 2
Measured and Estimated Flow Parameters, River Calder

Measurement		Measured		Estimated		Error				
Name	Date, Time	d_{meas} (m)	Q_{meas} (m^3/s)	d_{est} (m)	Q_{est} (m^3/s)	err_d (%)	err_Q (%)	F_{est} (−)	$k_0 d$ (−)	$k_0 L$ (−)
C01	13 October 2020, 14:30	0.19	0.56	0.19 ± 0.00	0.62 ± 0.01	4.7	12.0	0.71	2.3	49
C02	06 October 2020, 09:30	0.22	0.57	0.21 ± 0.01	0.75 ± 0.03	−2.8	30.2	0.74	2.1	39
C03	07 October 2020, 12:00	0.23	0.59	0.26 ± 0.02	0.98 ± 0.06	14.0	67.0	0.77	1.9	34
C04	11 October 2020, 12:15	0.24	0.76	0.22 ± 0.01	0.90 ± 0.04	−9.1	19.1	0.78	1.9	31
C05	09 October 2020, 12:00	0.27	0.79	0.37 ± 0.05	1.56 ± 0.20	38.0	98.6	0.78	1.9	28
C06	08 October 2020, 15:00	0.41	1.89	0.38 ± 0.03	2.26 ± 0.18	−6.5	19.8	0.89	1.4	14
C07	10 October 2020, 15:00	0.40	1.93	0.35 ± 0.07	2.00 ± 0.39	−13.8	3.7	0.87	1.5	15
C08	06 October 2020, 15:30	0.40	2.00	0.32 ± 0.03	1.81 ± 0.17	−20.9	−9.3	0.86	1.6	15
C09	08 October 2020, 12:30	0.49	2.89	0.55 ± 0.08	3.67 ± 0.54	12.9	27.0	0.92	1.3	11
C10	10 October 2020, 11:30	0.49	3.08	0.44 ± 0.09	3.01 ± 0.62	−10.9	−2.3	0.94	1.3	10
C11	10 October 2020, 09:30	0.60	3.75	0.52 ± 0.12	3.85 ± 0.91	−12.8	2.6	0.92	1.3	9
C12	08 October 2020, 09:00	0.69	4.71	0.67 ± 0.16	5.23 ± 1.29	−2.2	11.1	0.90	1.4	8

between measured and estimated discharge varied between 2.3% (C10) and 99% (C05), with most values below 30% and an rms difference of 37.6%. The expected uncertainties calculated with synthetic data were higher compared to the River Sheaf (14.6% for both d and Q), mainly because of the lower spectral resolution. For both rivers, the relative difference between the measured and estimated flow rates was large, close to 30% in average. The fact that the flow rate differences were larger than the depth differences are thought to be due to errors in the surface velocity and/or of the velocity index.

Figures 14 and 15 show the timeline of the measured and estimated flow depth and discharge, for the River Sheaf and for the River Calder, respectively. For the River Sheaf, only the measurements performed between 13 January and 23 March 2019 are shown. The measurements for both rivers show multiple depth and discharge peaks. The estimates of d and Q based on the analysis of videos follow the same distribution in time, with larger uncertainties near the peaks (between 12 March 2019 and 16 March 2019). The two highest peaks recorded on the River Calder occurred at night and no videos were available. For the River Sheaf, the peak values of the depth and discharge were overestimated (measurements S16, S17, and S14), while for the River Calder the largest error occurred in between the second and the third peak, during a lower flow (measurement C05).

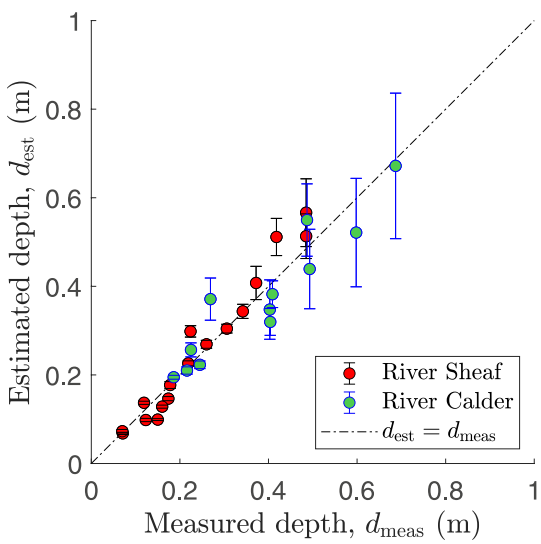

Figure 12. Water depth estimated from videos of the River Sheaf (red) and Calder (blue). The abscissa is the measured water depth, d_{meas}. The dashed line indicates $d_{est} = d_{meas}$. The error bars represent the uncertainty estimated with synthetic data.

7. Discussion

Based on the results in Section 6, uncertainty about the velocity index and the spectral resolution had the largest impact on the measurement accuracy. The velocity index is a source of uncertainty for all noncontact discharge measurements (Hauet et al., 2018; Welber et al., 2016). The spectral resolution was a limitation for the present study due to the presence of waves with a wavelength comparable to the width of the river. The large window did not allow to consider transverse variations of the flow velocity and depth. This could explain the overestimation of the discharge especially at high flows, for both rivers. The estimations of the discharge were found to be more accurate for the flow conditions with a larger aspect ratio, in agreement with the conclusions of the uncertainty analysis reported in Section 4. In wider rivers where width is not constrained and where the size of the measurement area can be increased relative to the water depth,

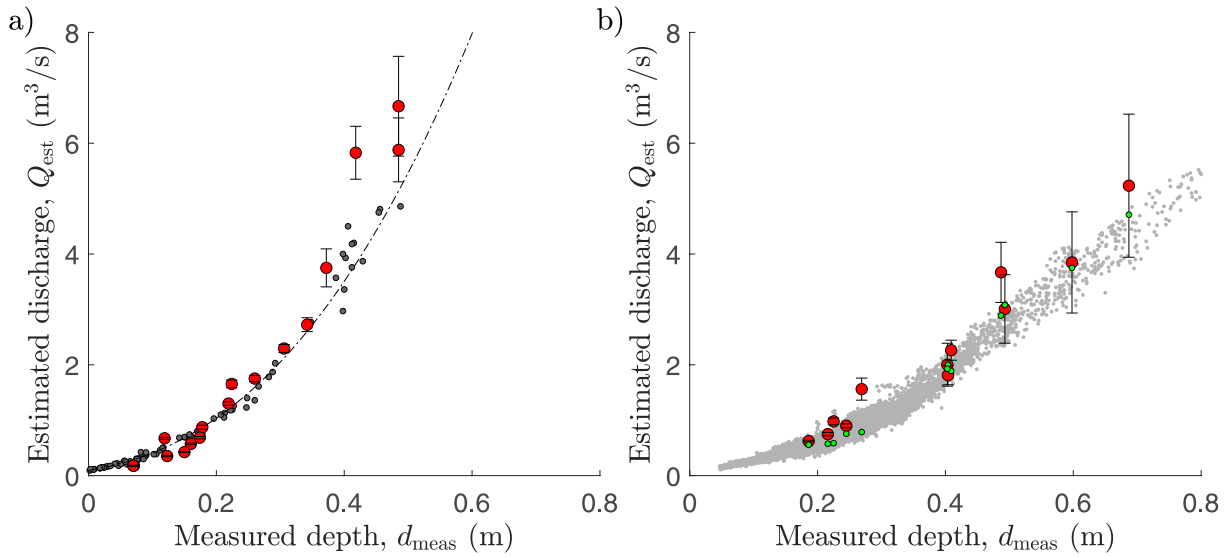

Figure 13. Flow rate estimated from videos of the (a) River Sheaf and (b) Calder. The red circles are obtained from the analysis of the videos, with the uncertainty estimated with synthetic data. In (a), the black circles indicate historical gauging surveys performed with acoustic Doppler current profilers (ADCPs) or propeller meters, and the black dashed line is a fitted power-function stage-discharge curve based on historical gauging. In (b) the gray circles indicate historical gauging surveys performed with an up-looking ADCP. Green circles show the ADCP measurements recorded at the same time of the videos.

the method should provide results with similar or lower uncertainties, provided the cameras have the required resolution and field of view.

The method described here is more suited to the monitoring of wide and shallow rivers and flows with finite Froude numbers. In principle, any water surface deformation observed in a river (including the patterns produced by the interaction with turbulence, and all types of GC waves including waves produced by wind or rain, wakes behind obstacles/vegetation, or stationary waves) will follow one of the dispersion relations presented in Section 2.2. Unlike other approaches such as large scale particle image velocimetry or surface Doppler velocime-

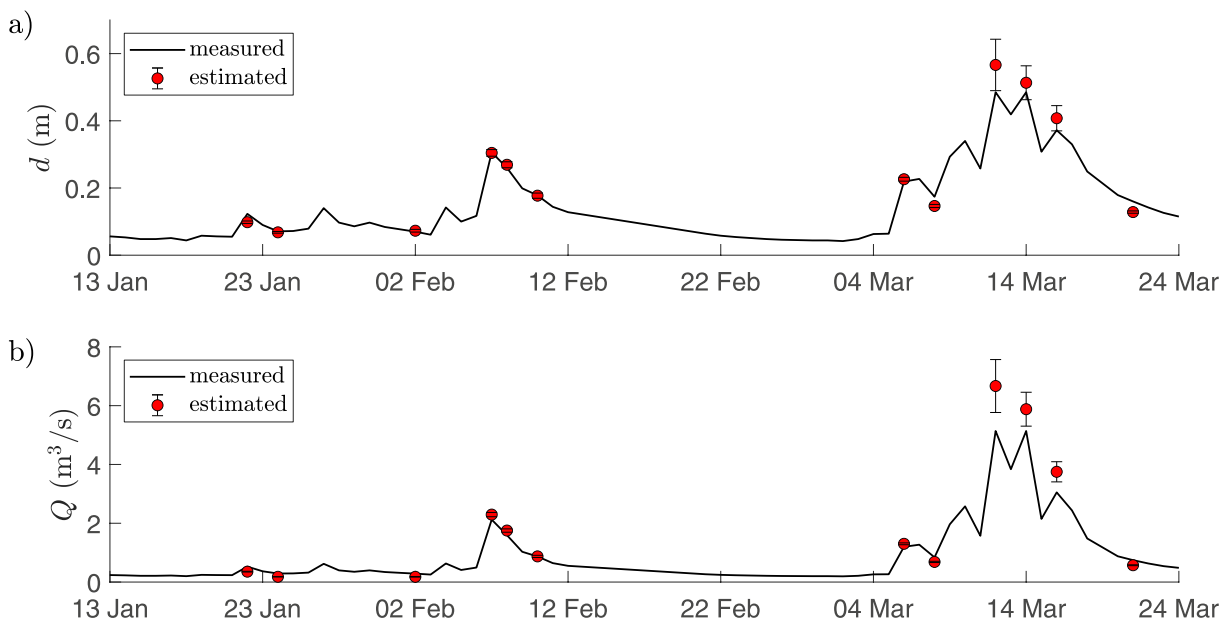

Figure 14. Temporal evolution of the measured (black line) and estimated (red circles) water (a) depth and (b) discharge of the River Sheaf, between 13 January and 23 March 2019. The measured discharge has been calculated by means of the fitted rating curve, as a function of the measured depth. The error bars represent the uncertainty estimated with synthetic data.

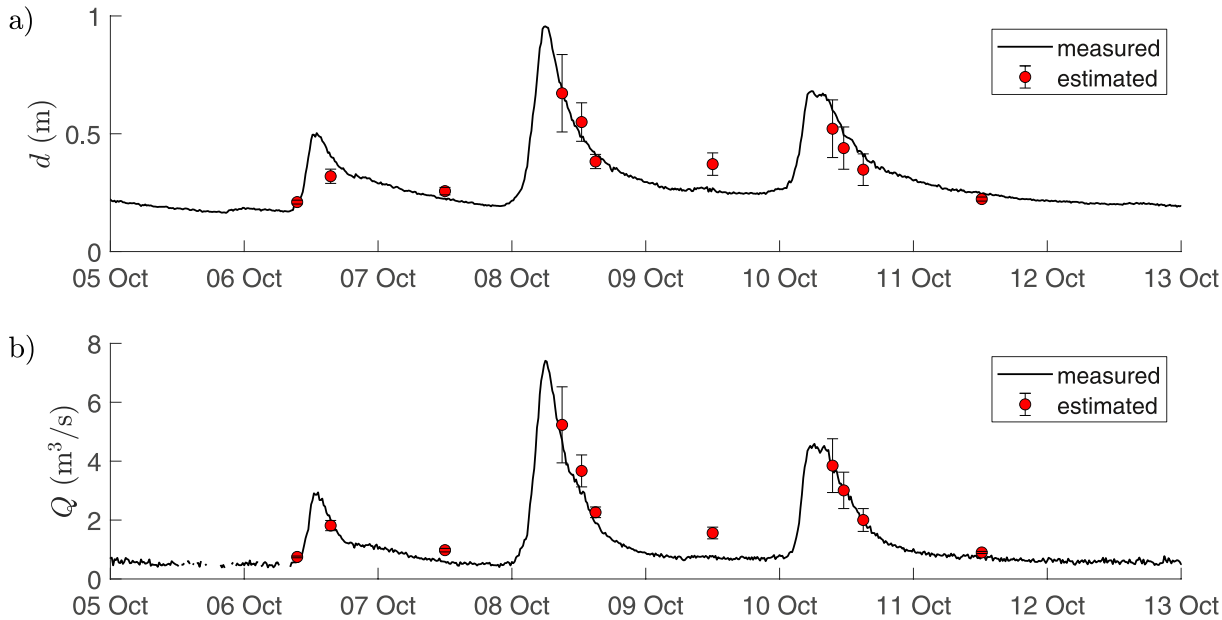

Figure 15. Temporal evolution of the measured (black line) and estimated (red circles) water (a) depth and (b) discharge of the River Calder, between 5 October and 13 October 2020. The error bars represent the uncertainty estimated with synthetic data.

try, the accuracy of the method proposed here is not reduced by the presence of GC waves (including stationary waves), but rather these waves enhance accuracy. Only the dispersion relation of GC waves depends on the water depth, therefore turbulence-generated patterns can only yield estimates of the flow velocity. Gravity waves can originate in the presence of wind, but they are also expected to occur without wind in a wide range of flow conditions, which includes a large proportion of river flows (Brocchini & Peregrine, 2001; Muraro et al., 2021). Most existing experimental and field investigations of the water surface dynamics have been performed in conditions where the water surface is predominantly "wavy" or "scarified" (Muraro et al., 2021). In shallow flows over a rough bed, where they seem to arise predominantly from the interaction with the bed roughness, GC waves have been observed directly or indirectly at Froude numbers between 0.15 and 0.95 (Muraro et al., 2021). At very low Froude numbers, however, these waves could be too short to allow an accurate estimation of the water depth (see the increase of the relative depth and discharge errors at the shallowest flows, in Figures 12 and 13). At Froude numbers near or above critical, on the other hand, the waves could become very long, and it could become impossible to ensure adequate spectral resolution (see the larger uncertainties at the deepest flows in Figures 12 and 13). The amplitude of turbulence-generated waves could change with the flow conditions following variations of the turbulence intensity (Valero, 2018; Valero & Bung, 2018). This would not be an issue since the proposed approach is able to clearly distinguish between turbulent waves and gravity-capillary waves because of their different dispersion behavior (Dolcetti et al., 2016). In the future, the link between the amplitude of turbulence-generated waves and the turbulence intensity in the flow could be used to improve the accuracy of the method or to gain additional information also about turbulence. There may also be cases where the shape of the bathymetry or some disturbance such as wind or vegetation causes a significant deviation of the velocity profile from the linear profile, or where localized and persistent large coherent turbulent structures modify the statistical behavior of the water surface. These cases would require the development of new dispersion relationships for water waves, which could be developed in the future.

It is useful to set some recommendation for the installation of the cameras, based on the experience obtained analyzing data for this work. First, any videos of the water surface must show some visible patterns that can be interpreted as an effect of deformations due to surface waves. Shadows from the river banks, bridges, trees, or other natural or man-made objects should be reduced, as well as direct sunlight reflection (sun-glint) which would saturate images. These optical effects can be mitigated by filtering and normalizing during preprocessing, but the overall quality of the analysis may still be affected. The camera should be stable, since camera movement produces an additional Doppler shift to the spectra. Nadir-looking cameras should be avoided, since water reflectance is minimal and waves are less visible from directly above. Therefore, fixed cameras may be prefera-

ble to cameras mounted on drones, or airplanes. If the camera is too close above the water surface, perspective distortion is large, and large water surface deformations could affect the accuracy of the orthorectification. Therefore, camera placement and resolution in relation to GC waves at low Froude numbers is important.

8. Conclusions

The aim of this work was to estimate river discharge using an entirely noncontact measurement technique, by exploiting the dependence of the water surface dynamics on the water depth and mean surface velocity. The implementation compares the spatiotemporal Fourier spectra of a sequence of rectified images of the water surface to a model of linear gravity-capillary waves and turbulence-generated surface deformations in a flow with a linear velocity profile. The approach is subject to a number of uncertainties, which depend on illumination conditions, resolution of the instrumentation, and validity of the model assumptions, and which were discussed in Section 4.

The applicability of the proposed method was tested on data collected in two rivers. The two sites represented field environments with conditions that should be consistent with the assumptions of the theoretical model used. The spectral analysis of the water surface revealed the simultaneous presence of gravity-capillary waves and surface deformations induced by turbulence, with a characteristic wavelength λ_0 that matched the theoretical wavelength of stationary waves. These observations are in agreement with previous laboratory experiments (Dolcetti et al., 2016).

The comparison between the flow parameters (water depth and discharge) estimated from the analysis of videos, and those expected or measured directly with alternative methods, confirmed the validity of the proposed approach but also highlighted its limitations. The water depth was estimated with an rms-average error of approximately $\pm$16% at both sites, which is considered a good outcome having been obtained with inexpensive fully noncontact methods. Discharge errors were larger, at 28% and 38% for the two sites, which was attributed to the uncertainty about the velocity index and spanwise variations of the flow velocity. Two aspects of the field implementation negatively affected measure performance: the weak dependence of the water surface dynamics on the depth, which requires the presence of waves with a wavelength much longer than the water depth and the need of a measurement area that is wide compared to the water surface wavelength. These requirements strongly limit the spatial resolution that can be obtained with the proposed approach. The issue could be addressed in the future using a multi-scale approach, where only the velocities are estimated at multiple spanwise locations.

Despite a growing interest by the scientific community, the research on the interaction between a turbulent flow and its free surface is still a relatively young and largely unexplored topic (Muraro et al., 2021). This work has confirmed the existence of a link between the water surface dynamics and macroscopic flow parameters such as surface velocity and water depth at a field scale, and has demonstrated the potential to monitor river discharge entirely remotely, with a physics-based approach. The main advantages of the proposed approach are that it requires the collection of images of the water surface alone; it does not require any other measurements (depth) or practical measures such as seeding of the flow with particles, which are problematic at high flood flows. It does not need any previous survey of the site other than for the purpose of projecting the images onto physical coordinates. These factors make this approach appealing especially for discharge estimation at previously ungauged sites, or for measurements during flood events, where access is unsafe, or at river reaches affected by frequent variations of bed level.

Appendix A: Fitting Algorithm

The Self-Adaptive Differential Evolution (SADE) algorithm (Qin & Suganthan, 2005) is a genetic optimization algorithm. The algorithm generates a number (for this work 20) of populations, or sets of parameters chosen randomly within a predetermined range. At each iteration, populations are modified according to different strategies, which are picked randomly with an initially identical probability. As the iterations progress, the probability to use each strategy changes according to the probability of success (i.e., the probability to increase the objective function) observed during the previous iterations. In this way, the algorithm is well suited for bringing to convergence even complex nonlinear problems with multiple parameters.

In order to give equal weight to the different types of waves that appear in the spectrum which have a relatively large dynamic range, the data were preprocessed as follows: The spectrum at each frequency $I_{p,q,n}$ was divided by its sum over the wavenumber indices, $\sum_p \sum_q I_{p,q,n}$, to compensate for the decay with frequency (normalization).

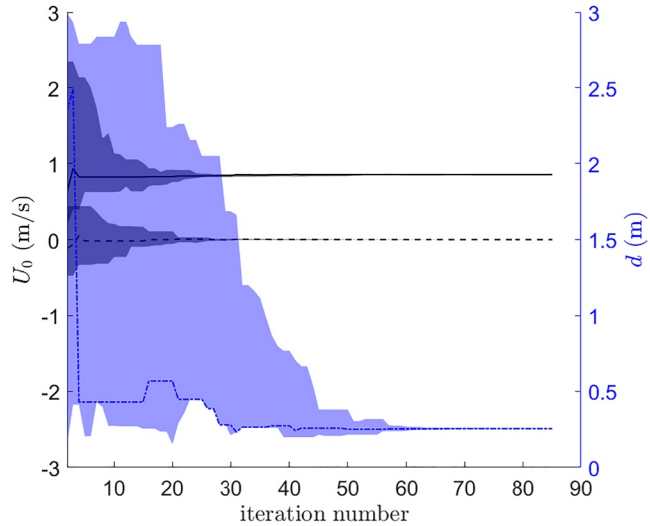

Figure A1. Example of convergence plot, based on flow conditions S11. The margins of the colored areas indicate the maximum and minimum of d (light blue) and of the two components of $\mathbf{U_0}$ (dark blue), across all populations, at each iteration. The lines indicate the values of d (dashed dotted, blue) and of the two components of $\mathbf{U_0}$ (solid black is the x_1 component, dashed black is the x_2 component) of the population with the highest Normalized Scalar Product at each iteration.

Then, the noise floor was removed by neglecting all elements of the matrix that were smaller than twice the average over the frequency index n of the normalized spectrum, $<2\,\langle \mathrm{I}_{p,q,n}\rangle_n$ (de-noising).

The SADE algorithm requires the definition of a search region for each parameter. For this work, it was assumed that U_1, $U_2 \in [-3, 3]$ m/s, $d \in [0, 3]$ m. The optimization algorithm was initialized with a set of 10 populations, each with a random combination of the three target parameters. The calculation was stopped when all populations had converged to the same maximum value of the NSP, within 10^{-5}%. The whole procedure was repeated 5 times, and the best-fit solution was identified as the result of the run with the highest value of the NSP.

An example of convergence plot, calculated for one single run based on flow condition S11, is shown in Figure A1. The estimation of each of the two components of the flow velocity converged more rapidly, in about 30 iterations, while the estimation of the water depth converged after about 60 iterations. This was due to the lower sensitivity of the dispersion relations to depth variations, as discussed in Section 4.

Appendix B: Sensitivity to Flow Speed and Depth Variations

The following equations represent the nondimensionalized sensitivity of the wave frequency with respect to the flow speed and depth, ξ_{U_0} and ξ_d, respectively, calculated from Equation 6

$$\xi_{U_0} = \sqrt{\frac{d}{g}}U_0\left(\frac{\partial\Omega_{\mathrm{GW}}}{\partial U_0}\right) = \left\{1 - \frac{m}{2}\frac{\tanh(kd)}{kd}\left[1 \mp \frac{\chi}{\sqrt{1+\chi^2}}\right]\right\} kd\mathsf{F}\cos(\theta); \tag{B1}$$

$$\xi_d = \sqrt{\frac{d^3}{g}}\left(\frac{\partial\Omega_{\mathrm{GW}}}{\partial d}\right) = kd\sqrt{\frac{(1+\mathsf{B})}{\mathsf{B}}\frac{kd}{\tanh(kd)}} \times\left\{\left[\frac{\tanh(kd)}{kd} - \frac{1}{\cosh^2(kd)}\right]\left(1 \mp \frac{\chi}{\sqrt{1+\chi^2}}\right)\chi \pm \frac{1}{2\cosh^2(kd)}\frac{1}{\sqrt{1+\chi^2}}\right\}, \tag{B2}$$

where

$$\chi = \frac{m}{2}\mathsf{F}\cos(\theta)\sqrt{\frac{\mathsf{B}}{(1+\mathsf{B})}\frac{\tanh(kd)}{kd}}, \tag{B3}$$

θ is the angle between $\mathbf{k}$ and $\mathbf{F}$, and $\sqrt{g/d}$ is a characteristic frequency used for the nondimensionalization.

Data Availability Statement

Data sets for this research are openly available at the following https://doi.org/10.5281/zenodo.6553739 (Perks et al., 2022).

Acknowledgments
The authors would like to thank T. Adams, L. Marshall, C. Shaw (UK Environment Agency), and F. Muraro (The University of Sheffield) for the help with setting up the camera and performing field measurements in the River Sheaf, H. Camfield (UK Environment Agency) for sharing the gauging data, and N. Everard (UK Centre for Ecology and Hydrology) for enabling the collaboration between the authors. Public sector information was licensed under the Open Government License v3.0. G. Dolcetti was funded by the UK Engineering and Physical Sciences Research Council Grant No. EP/R022275/1. B. Hortobágyi was funded by the UK Natural Environment Research Council Grant No. NE/K008781/1 "Susceptibility of catchments to INTense RAinfall and flooding (SINATRA)." Instrumentation was funded by the UK Environment Agency through M. Perks.

References

Almar, R., Bergsma, E. W. J., Catalan, P. A., Cienfuegos, R., Suarez, L., Lucero, F., et al. (2021). Sea state from single optical images: A methodology to derive wind-generated ocean waves from cameras, drones and satellites. *Remote Sensing*, *13*(4), 679. https://doi.org/10.3390/rs13040679

Bell, P. S. (1999). Shallow water bathymetry derived from an analysis of X-band marine radar images of waves. *Coastal Engineering*, *37*(3–4), 513–527. https://doi.org/10.1016/s0378-3839(99)00041-1

Benetazzo, A., Bergamasco, F., Yoo, J., Cavaleri, L., Kim, S.-S., Bertotti, L., et al. (2018). Characterizing the signature of a spatio-temporal wind wave field. *Ocean Modelling*, *129*, 104–123. https://doi.org/10.1016/j.ocemod.2018.06.007

Biésel, F. (1950). *Etude théorique de la houle en eau courante* (Vol. 5A, pp. 279–285). La Houille Blanche. https://doi.org/10.1051/lhb/1950009

Bradley, A. A., Kruger, A., Meselhe, E. A., & Muste, M. V. I. (2002). Flow measurement in streams using video imagery. *Water Resources Research*, *38*(12), 51. https://doi.org/10.1029/2002wr001317

Brocchini, M., & Peregrine, D. H. (2001). The dynamics of strong turbulence at free surfaces. Part 1. Description. *Journal of Fluid Mechanics*, *449*, 225–254. https://doi.org/10.1017/s0022112001006012

Campana, J., Terrill, E. J., & De Paolo, T. (2016). The development of an inversion technique to extract vertical current profiles from X-band radar observations. *Journal of Atmospheric and Oceanic Technology*, *33*(9), 2015–2028. https://doi.org/10.1175/jtech-d-15-0145.1

Chanson, H. (2000). Boundary shear stress measurements in undular flows: Application to standing wave bed forms. *Water Resources Research*, *36*(10), 3063–3076. https://doi.org/10.1029/2000wr900154

Detert, M., Johnson, E. D., & Weitbrecht, V. (2017). Proof-of-concept for low-cost and non-contact synoptic airborne river flow measurements. *International Journal of Remote Sensing*, *38*(8–10), 2780–2807. https://doi.org/10.1080/01431161.2017.1294782

Dolcetti, G., & García Nava, H. (2019a). Wavelet spectral analysis of the free surface of turbulent flows by Giulio Dolcetti and Héctor García Nava. *Journal of Hydraulic Research*, *57*(4), 604–606. https://doi.org/10.1080/00221686.2018.1555561

Dolcetti, G., & García Nava, H. (2019b). Wavelet spectral analysis of the free surface of turbulent flows. *Journal of Hydraulic Research*, *57*(2), 211–226. https://doi.org/10.1080/00221686.2018.1478896

Dolcetti, G., Horoshenkov, K. V., Krynkin, A., & Tait, S. J. (2016). Frequency-wavenumber spectrum of the free surface of shallow turbulent flows over a rough boundary. *Physics of Fluids*, *28*(10), 105105. https://doi.org/10.1063/1.4964926

Dolcetti, G., Hortobágyi, B., Perks, M., & Tait, S. J. (2020). The effect of surface gravity waves on the measurement of river surface velocity. In *River flow 2020* (pp. 862–871). CRC Press. https://doi.org/10.1201/b22619-122

Dolcetti, G., & Krynkin, A. (2017). Doppler spectra of airborne ultrasound forward scattered by the rough surface of open channel turbulent water flows. *Journal of the Acoustical Society of America*, *142*(5), 3122–3134. https://doi.org/10.1121/1.5011183

Dolcetti, G., Krynkin, A., & Horoshenkov, K. V. (2017). Doppler spectra of airborne sound backscattered by the free surface of a shallow turbulent water flow. *Journal of the Acoustical Society of America*, *142*(6), 3387–3401. https://doi.org/10.1121/1.5015990

Dugan, J. P., Piotrowski, C. C., & Williams, J. Z. (2001). Water depth and surface current retrievals from airborne optical measurements of surface gravity wave dispersion. *Journal of Geophysical Research*, *106*(C8), 16903–16915. https://doi.org/10.1029/2000jc000369

Ellingsen, S. Å., & Li, Y. (2017). Approximate dispersion relations for waves on arbitrary shear flows. *Journal of Geophysical Research: Oceans*, *122*(12), 9889–9905. https://doi.org/10.1002/2017jc012994

Eltner, A., Elias, M., Sardemann, H., & Spieler, D. (2018). Automatic image-based water stage measurement for long-term observations in ungauged catchments. *Water Resources Research*, *54*(12), 10–362. https://doi.org/10.1029/2018wr023913

Fenton, J. D. (1973). Some results for surface gravity waves on shear flows. *IMA Journal of Applied Mathematics*, *12*(1), 1–20. https://doi.org/10.1093/imamat/12.1.1

Fujita, I., & Tsubaki, R. (2002). A novel free-surface velocity measurement method using spatio-temporal images. In *Hydraulic measurements and experimental methods 2002*, Estates Park. 1–7. https://doi.org/10.1061/40655(2002)85

Gharahjeh, S., & Aydin, I. (2016). Application of video imagery techniques for low cost measurement of water surface velocity in open channels. *Flow Measurement and Instrumentation*, *51*, 79–94. https://doi.org/10.1016/j.flowmeasinst.2016.09.001

Hauet, A., Morlot, T., & Daubagnan, L. (2018). *Velocity profile and depth-averaged to surface velocity in natural streams: A review over a large sample of rivers*. In *E3s web of conferences* (Vol. 40). 06015. https://doi.org/10.1051/e3sconf/20184006015

Holman, R., Plant, N., & Holland, T. (2013). cBathy: A robust algorithm for estimating nearshore bathymetry. *Journal of Geophysical Research: Oceans*, *118*(5), 2595–2609. https://doi.org/10.1002/jgrc.20199

Jin, T., & Liao, Q. (2019). Application of large scale PIV in river surface turbulence measurements and water depth estimation. *Flow Measurement and Instrumentation*, *67*, 142–152. https://doi.org/10.1016/j.flowmeasinst.2019.03.001

Johnson, E. D., & Cowen, E. A. (2016). Remote monitoring of volumetric discharge employing bathymetry determined from surface turbulence metrics. *Water Resources Research*, *52*(3), 2178–2193. https://doi.org/10.1002/2015wr017736

Krynkin, A., Horoshenkov, K. V., & Van Renterghem, T. (2016). An airborne acoustic method to reconstruct a dynamically rough flow surface. *Journal of the Acoustical Society of America*, *140*(3), 2064–2073. https://doi.org/10.1121/1.4962559

Lamb, H. (1945). *Hydrodynamics* (6th edn). Dover Publications Inc.

Le Coz, J., Hauet, A., Pierrefeu, G., Dramais, G., & Camenen, B. (2010). Performance of image-based velocimetry (LSPIV) applied to flash-flood discharge measurements in Mediterranean rivers. *Journal of Hydrology*, *394*(1–2), 42–52. https://doi.org/10.1016/j.jhydrol.2010.05.049

Longuet-Higgins, M. S. (1996). Surface manifestations of turbulent flow. *Journal of Fluid Mechanics*, *308*, 15–29. https://doi.org/10.1017/s0022112096001371

Lund, B., Graber, H. C., Tamura, H., Collins, C. O., III, & Varlamov, S. M. (2015). A new technique for the retrieval of near-surface vertical current shear from marine X-band radar images. *Journal of Geophysical Research: Oceans*, *120*(12), 8466–8486. https://doi.org/10.1002/2015jc010961

Messerli, A., & Grinsted, A. (2015). Image georectification and feature tracking toolbox: ImGRAFT. *Geoscientific Instrumentation, Methods and Data Systems*, *4*(1), 23. https://doi.org/10.5194/gi-4-23-2015

Moramarco, T., Barbetta, S., Bjerklie, D. M., Fulton, J. W., & Tarpanelli, A. (2019). River bathymetry estimate and discharge assessment from remote sensing. *Water Resources Research*, *55*(8), 6692–6711. https://doi.org/10.1029/2018wr024220

Muraro, F., Dolcetti, G., Nichols, A., Tait, S. J., & Horoshenkov, K. V. (2021). Free-surface behaviour of shallow turbulent flows. *Journal of Hydraulic Research*, *59*(1), 1–20. https://doi.org/10.1080/00221686.2020.1870007

Muste, M., Fujita, I., & Hauet, A. (2008). Large-scale particle image velocimetry for measurements in riverine environments. *Water Resources Research*, *44*(4). https://doi.org/10.1029/2008wr006950

Muste, M., Schöne, J., & Creutin, J.-D. (2005). Measurement of free-surface flow velocity using controlled surface waves. *Flow Measurement and Instrumentation*, *16*(1), 47–55. https://doi.org/10.1016/j.flowmeasinst.2004.08.003

National River Flow Archive. (2020). 27067—Sheaf at highfield road. Retrieved from https://nrfa.ceh.ac.uk/data/station/meanflow/27067/

Nezu, I., & Nakagawa, H. (1993). *Turbulence in open channel flows*, Balkema.

Perks, M. T., Hortobágyi, B., Dolcetti, G., & Tait, S. (2022). Sequences of orthorectified images of the water surface of two rivers: River Sheaf (Sheffield, UK), and River Calder (Todmorden, UK) [Dataset]. Zenodo, https://doi.org/10.5281/zenodo.6553739

Perks, M. T., Russell, A. J., & Large, A. R. G. (2016). Advances in flash flood monitoring using unmanned aerial vehicles (UAVs). *Hydrology and Earth System Sciences*, *20*(10), 4005–4015. https://doi.org/10.5194/hess-20-4005-2016

Piotrowski, C. C., & Dugan, J. P. (2002). Accuracy of bathymetry and current retrievals from airborne optical time-series imaging of shoaling waves. *IEEE Transactions on Geoscience and Remote Sensing*, *40*(12), 2606–2618. https://doi.org/10.1109/tgrs.2002.807578

Plant, W. J., Keller, W. C., & Hayes, K. (2005). Measurement of river surface currents with coherent microwave systems. *IEEE Transactions on Geoscience and Remote Sensing*, *43*(6), 1242–1257. https://doi.org/10.1109/tgrs.2005.845641

Qin, A. K., & Suganthan, P. N. (2005). Self-adaptive differential evolution algorithm for numerical optimization. *2005 IEEE Congress on Evolutionary Computation*, *2*, 1785–1791. https://doi.org/10.1109/CEC.2005.1554904

Salameh, E., Frappart, F., Almar, R., Baptista, P., Heygster, G., & Lubac, B. (2019). Monitoring beach topography and nearshore bathymetry using spaceborne remote sensing: A review. *Remote Sensing*, *11*(19), 2212. https://doi.org/10.3390/rs11192212

Sarpkaya, T. (1996). Vorticity, free surface, and surfactants. *Annual Review of Fluid Mechanics*, *28*(1), 83–128. https://doi.org/10.1146/annurev.fl.28.010196.000503

Savelsberg, R., & Van De Water, W. (2009). Experiments on free-surface turbulence. *Journal of Fluid Mechanics*, *619*, 95–125. https://doi.org/10.1017/s0022112008004369

Senet, C. M., Seemann, J., & Ziemer, F. (2001). The near-surface current velocity determined from image sequences of the sea surface. *IEEE Transactions on Geoscience and Remote Sensing*, *39*(3), 492–505. https://doi.org/10.1109/36.911108

Serafino, F., Lugni, C., & Soldovieri, F. (2009). A novel strategy for the surface current determination from marine X-band radar data. *IEEE Geoscience and Remote Sensing Letters*, *7*(2), 231–235. https://doi.org/10.1109/LGRS.2009.2031878

Shen, C., Huang, W., Gill, E. W., Carrasco, R., & Horstmann, J. (2015). An algorithm for surface current retrieval from X-band marine radar images. *Remote Sensing*, *7*(6), 7753–7767. https://doi.org/10.3390/rs70607753

Smeltzer, B. K., Æsøy, E., Ådnøy, A., & Ellingsen, S. Å. (2019). An improved method for determining near-surface currents from wave dispersion measurements. *Journal of Geophysical Research: Oceans*, *124*(12), 8832–8851. https://doi.org/10.1029/2019JC015202

Smith, M., Vericat, D., & Gibbins, C. (2012). Through-water terrestrial laser scanning of gravel beds at the patch scale. *Earth Surface Processes and Landforms*, *37*(4), 411–421. https://doi.org/10.1002/esp.2254

Spicer, K. R., Costa, J. E., & Placzek, G. (1997). Measuring flood discharge in unstable stream channels using ground-penetrating radar. *Geology*, *25*(5), 423–426. https://doi.org/10.1130/0091-7613(1997)025<0423:mfdius>2.3.co;2

Stewart, R. H., & Joy, J. W. (1974). HF radio measurements of surface currents. *Deep-Sea Research and Oceanographic Abstracts*, *21*(12), 1039–1049. https://doi.org/10.1016/0011-7471(74)90066-7

Stilwell, D. J. (1969). Directional energy spectra of the sea from photographs. *Journal of Geophysical Research*, *74*(8), 1974–1986. https://doi.org/10.1029/jb074i008p01974

Streßer, M., Carrasco, R., & Horstmann, J. (2017). Video-based estimation of surface currents using a low-cost quadcopter. *IEEE Geoscience and Remote Sensing Letters*, *14*(11), 2027–2031. https://doi.org/10.1109/LGRS.2017.2749120

Tauro, F., Piscopia, R., & Grimaldi, S. (2017). Streamflow observations from cameras: Large-scale particle image velocimetry or particle tracking velocimetry? *Water Resources Research*, *53*(12), 10374–10394. https://doi.org/10.1002/2017wr020848

Tauro, F., Porfiri, M., & Grimaldi, S. (2014). Orienting the camera and firing lasers to enhance large scale particle image velocimetry for streamflow monitoring. *Water Resources Research*, *50*(9), 7470–7483. https://doi.org/10.1002/2014wr015952

Teixeira, M. A. C. (2019). Wavelet spectral analysis of the free surface of turbulent flows by Giulio Dolcetti and Héctor García Nava. *Journal of Hydraulic Research*, *57*(4), 603–604. https://doi.org/10.1080/00221686.2018.1555560

Teixeira, M. A. C., & Belcher, S. E. (2006). On the initiation of surface waves by turbulent shear flow. *Dynamics of Atmospheres and Oceans*, *41*(1), 1–27. https://doi.org/10.1016/j.dynatmoce.2005.10.001

Valero, D. (2018). *On the fluid mechanics of self-aeration in open channel flows*, Doctoral dissertation. https://hdl.handle.net/2268/229191

Valero, D., & Bung, D. B. (2018). Reformulating self-aeration in hydraulic structures: Turbulent growth of free surface perturbations leading to air entrainment. *International Journal of Multiphase Flow*, *100*, 127–142. https://doi.org/10.1016/j.ijmultiphaseflow.2017.12.011

Welber, M., Le Coz, J., Laronne, J. B., Zolezzi, G., Zamler, D., Dramais, G., et al. (2016). Field assessment of noncontact stream gauging using portable surface velocity radars (SVR). *Water Resources Research*, *52*(2), 1108–1126. https://doi.org/10.1002/2015wr017906

Williams, W. W. (1947). The determination of gradients on enemy-held beaches. *The Geographical Journal*, *109*(1/3), 76–90. https://doi.org/10.2307/1789903

Woodget, A. S., Carbonneau, P. E., Visser, F., & Maddock, I. P. (2015). Quantifying submerged fluvial topography using hyperspatial resolution UAS imagery and structure from motion photogrammetry. *Earth Surface Processes and Landforms*, *40*(1), 47–64. https://doi.org/10.1002/esp.3613

Yang, Y., Wen, B., Wang, C., & Hou, Y. (2019). Two-dimensional velocity distribution modeling for natural river based on UHF radar surface current. *Journal of Hydrology*, *577*, 123930. https://doi.org/10.1016/j.jhydrol.2019.123930

Young, D. S., Hart, J. K., & Martinez, K. (2015). Image analysis techniques to estimate river discharge using time-lapse cameras in remote locations. *Computers & Geosciences*, *76*, 1–10. https://doi.org/10.1016/j.cageo.2014.11.008

Young, I. R., Rosenthal, W., & Ziemer, F. (1985). A three-dimensional analysis of marine radar images for the determination of ocean wave directionality and surface currents. *Journal of Geophysical Research*, *90*(C1), 1049–1059. https://doi.org/10.1029/jc090ic01p01049

Zakharov, V. E., & Shrira, V. I. (1990). Formation of the angular spectrum of wind waves. *Journal of Experimental and Theoretical Physics*, *71*, 1091–1100. http://jetp.ras.ru/cgi-bin/e/index/e/71/6/p1091?a=list